Journal of Energy Chemistry 95 (2024) 364–379

Contents lists available at ScienceDirect

Journal of Energy Chemistry

journal homepage: www.elsevier.com/locate/jechem

http://www.journals.elsevier.com/journal-of-energy-chemistry/

Characterization and quantification of multi-field coupling in lithium-ion batteries under mechanical constraints

Xue Cai [a,b,c,d], Caiping Zhang [a,*], Zeping Chen [a], Linjing Zhang [a], Dirk Uwe Sauer [b,c,d,e], Weihan Li [b,c,d,*]

[a] National Active Distribution Network Technology Research Center, Beijing Jiaotong University, Beijing 100044, China
[b] Chair for Electrochemical Energy Conversion and Storage Systems, Institute for Power Electronics and Electrical Drives (ISEA), RWTH Aachen University, Campus Boulevard 89, 52074 Aachen, Germany
[c] Center for Ageing, Reliability and Lifetime Prediction of Electrochemical and Power Electronic Systems (CARL), Campus-Boulevard 89, 52074 Aachen, Germany
[d] Juelich Aachen Research Alliance, JARA-Energy, Aachen, Germany
[e] Helmholtz Institute Münster (HI MS), IEK-12, Forschungszentrum Jülich, Germany

ARTICLE INFO

Article history:
Received 15 February 2024
Revised 23 March 2024
Accepted 25 March 2024
Available online 4 April 2024

Keywords:
Lithium-ion battery
Muti-field coupling
Mechanical constraints
Interaction mechanisms
Quantitative analysis

ABSTRACT

The safety and durability of lithium-ion batteries under mechanical constraints depend significantly on electrochemical, thermal, and mechanical fields in applications. Characterizing and quantifying the multi-field coupling behaviors requires interdisciplinary efforts. Here, we design experiments under mechanical constraints and introduce an in-situ analytical framework to clarify the complex interaction mechanisms and coupling degrees among multi-physics fields. The proposed analytical framework integrates the parameterization of equivalent models, in-situ mechanical analysis, and quantitative assessment of coupling behavior. The results indicate that the significant impact of pressure on impedance at low temperatures results from the diffusion-controlled step, enhancing kinetics when external pressure, like 180 to 240 kPa at 10 °C, is applied. The diversity in control steps for the electrochemical reaction accounts for the varying impact of pressure on battery performance across different temperatures. The thermal expansion rate suggests that the swelling force varies by less than 1.60% per unit of elevated temperature during the lithiation process. By introducing a composite metric, we quantify the coupling correlation and intensity between characteristic parameters and physical fields, uncovering the highest coupling degree in electrochemical-thermal fields. These results underscore the potential of analytical approaches in revealing the mechanisms of interaction among multi-fields, with the goal of enhancing battery performance and advancing battery management.
© 2024 Science Press and Dalian Institute of Chemical Physics, Chinese Academy of Sciences. Published by ELSEVIER B.V. and Science Press. This is an open access article under the CC BY-NC-ND license (http://creativecommons.org/licenses/by-nc-nd/4.0/).

1. Introduction

To facilitate the large-scale adoption of electric vehicles and electrochemical energy storage stations for a sustainable, resource-conserving, and environment-friendly energy economy, lithium-ion batteries (LIBs) are widely used due to their high energy density, cost-effectiveness, and long lifespan [1]. In vehicle applications, battery cells are assembled into modules or packs under stack pressure and combined with cooling, control, and buffer elements via mechanical jointing. These assemblies are then mounted onto the vehicle chassis (rigid frames) [2–5]. As a result, LIBs usually operate under initial preload conditions and mechanical constraints. In this context, LIBs undergo electrochemical reactions accompanied by lithiation/delithiation-induced expansion force and elevated temperatures due to sustainable heat generation [2]. Expansion and preload force under mechanical constraints result in mechanical stress, which affects the contact surface area, porosity, ionic conductivity, and heat generation, leading to varied electrochemical-thermal behavior within the cell [6,7]. Heat generation also affects swelling responses [8,9], electrolyte conductivity, and diffusivity [10], thereby altering the mechanical-electrochemical behavior of the cell [11,12]. These interconnected behaviors collectively influence the practical performance of LIBs. Furthermore, overlooking thermal and mechanical effects in battery management systems (BMSs) may lead to inaccurate state estimation and lifetime prediction. Therefore, understanding the intrinsic mechanisms of battery multi-field coupling is crucial for improving performance and developing effective BMS algorithms.

* Corresponding authors.
E-mail addresses: zhangcaiping@bjtu.edu.cn (C. Zhang), weihan.li@isea.rwth-aachen.de (W. Li).

https://doi.org/10.1016/j.jechem.2024.03.048
2095-4956/© 2024 Science Press and Dalian Institute of Chemical Physics, Chinese Academy of Sciences. Published by ELSEVIER B.V. and Science Press.
This is an open access article under the CC BY-NC-ND license (http://creativecommons.org/licenses/by-nc-nd/4.0/).

Focusing on pressurized battery cells in packs, previous studies have investigated single mechanical responses and mechanical-related field coupling behaviors using specific test platforms [8,13–21]. These platforms fall into three categories: free stack mode (FSM) [13,15,17], constant pressure mode (CPM) [14,16], and constant displacement mode (CDM) [18–20]. Each platform has distinct advantages and limitations. For instance, FSM can measure swelling displacement and temperature at single or multiple points on the cell surface [8,13] but cannot replicate the actual pressurized state of LIBs within battery packs. CPM can measure lithiation/delithiation-induced swelling displacement of LIBs under preset stack pressures. However, it faces limitations in arranging thermocouples on the cell surface due to the plates [16]. Similarly, CDM encounters challenges with temperature acquisition. With a fixed expansion space, it can only measure the total swelling force on contact surfaces during the charge and discharge process using load cells [18,20] or thin-film pressure sensors [19]. Therefore, to investigate multi-field coupling issues effectively, it is crucial to leverage the strengths of each test platform. Conducting well-designed experiments under existing test platforms is necessary to systematically explore the interaction mechanisms among multiple fields.

Understanding the intricate coupling mechanisms requires a detailed exploration of the underlying electrochemical nature at a mechanistic level. Parameterization is valuable in visualizing coupling behaviors, unveiling interactions, and quantifying multi-field coupling effects. Existing studies on parameterization have primarily focused on electrochemical models (EMs) [2,10,21–24] and equivalent circuit models (ECMs) [7,25–28]. While EMs involve partial differential equations and numerous parameters, ECMs, characterized by fewer parameters, offer notable advantages in analyzing multi-field coupling behaviors. In the realm of electrochemical behavior, impedance parameters from the non-invasive electrochemical impedance spectrum (EIS) have been instrumental in unveiling predominant electrochemical processes affected by specific factors [29]. For instance, pressure-induced effects have been observed, such as shortening the electron transport path, elongating the ionic transport distance, and increasing the active material surface area. However, investigations into pressure-induced electrochemical mechanisms have been limited to room temperature. Although correlations between impedance parameters and temperatures following Arrhenius behavior have been reported [11,30,31], these have been predominantly studied in the unpressurized state. As of present knowledge, no studies have explored the impact of mechanical stress on the electrochemical behavior of LIBs across a broad temperature spectrum. Notably, in the Bernardi equation [32], the irreversible heat generated by impedance parameters plays a crucial role in influencing the rate of temperature rise (TR). The sustained TR during high-current charge or discharge contributes to cell thermal expansion and contraction, directly impacting the mechanical behavior of LIBs [8]. These mechanical aspects, including swelling displacement, force, and elastic modulus calculated by Hook's law [13], are subject to influences from various factors such as initial stress, state of charge (SOC), C-rate, and more. Particularly in silicon-containing cells, distinct phase transition paths between a-$Li_{15}Si_{14}$ and c-$Li_{15}Si_{14}$ during charge and discharge processes result in a notable hysteresis effect on voltage and mechanical behavior [33–35]. Hence, mechanical properties originating from phase transitions are closely linked to cell chemistry, further emphasizing their interdependence.

Analytical approaches for mechanical behavior are broadly categorized as ex-situ and in-situ methods. Ex-situ methods, including X-ray diffraction [36–38] and dilatometry [39–42], are commonly used to measure single-electrode swelling. However, these methods come with limitations, requiring experienced researchers to customize cells and facing challenges in matching measurements across different scales, as demonstrated in the work by Pegel et al. [40]. On the other hand, differential analysis, an in-situ analytical approach [43,44], establishes connections between electrochemical and mechanical properties. Yet, the lack of electrode-scale information hinders an in-depth investigation of the involved electrochemical reactions. Therefore, developing in-situ mechanical characterization is critical to enabling non-invasive, cross-scale analysis to elucidate the electrochemical aspects of mechanical behavior influenced by various factors.

In multi-field coupling problems, pioneering research endeavors have concentrated on two physical fields to investigate intricate interactions among them, e.g., the coupling of electrochemical-mechanical [40,41,45] and thermal-mechanical fields [8,46]. Diffusion-induced stress has been demonstrated to be SOC-dependent [40] and thermal-dependent [45]. The non-uniform thermal expansion stems from uneven thermal stresses arising from disparate current distribution and charging rates [46]. Most recently, multi-field coupling problems were investigated in a weakly coupled approach [2,11,21], i.e., free mechanical boundary and one-way coupled between parameters and physical fields. Nevertheless, identifying parameters with high correlations to specific physical fields remains unresolved. A discussion surrounding which parameters are more significantly influenced by specific physical fields is yet to be addressed. This calls for the development of methods capable of quantitatively assessing correlations and strengths within multi-field coupling, addressing these inquiries. Controlling coupled degrees through quantitative analysis improves the electrochemical performance and mechanical stability of LIBs. Furthermore, BMS algorithms that consider the coupling effect enhance the accuracy and reliability of state estimation and prediction.

To address the existing research gaps, we aim to explore the nature of multi-physics coupling under mechanical constraints by designing comprehensive experiment matrices and developing an in-situ quantitative analytical framework. The schematic overview of the proposed approach is displayed in Fig. 1. Considering the advantages and limitations of various mechanical constraints, i.e., FSM, CPM, and CDM, for operando temperature and swelling measurements, we conducted a series of characterization tests. These included charge/discharge tests under CPM, thermal swelling under FSM and CDM, and EIS tests under CDM. This approach, rooted in mechanical constraints, facilitated the isolation of temperature and external pressure effects on battery electrochemical-mechanical performance. Our study covered a broad spectrum of mechanical constraints, temperatures, and external pressures, providing a holistic understanding of multi-field coupling in LIBs. To comprehend the electrochemical nature of multi-field coupling without disassembling cells, we formulated an in-situ quantitative analytical framework. This framework integrates the parameterization of multi-field coupling behavior, characterization of mechanical behavior, and their quantitative assessment. It unveils interaction and correlation mechanisms among different fields, quantifying the intensity of their coupling. Leveraging characteristic parameters from equivalent models, we visualized and described coupling behaviors, extracting essential physical information. We unveiled the influence of mechanical stress on thermodynamic and kinetic mechanisms across diverse temperatures through electrochemical parameters, elucidating the primary factors behind the variations in capacity and resistance performance and heat generation rate of LIBs. Additionally, we explored the effects of temperature and pressure on mechanical behavior using pertinent mechanical parameters. Analyzing differential voltage and swelling curves allowed us to probe the electrochemical origins of mechanical behavior, attributing thermal and pressure effects to lattice structure transformations.

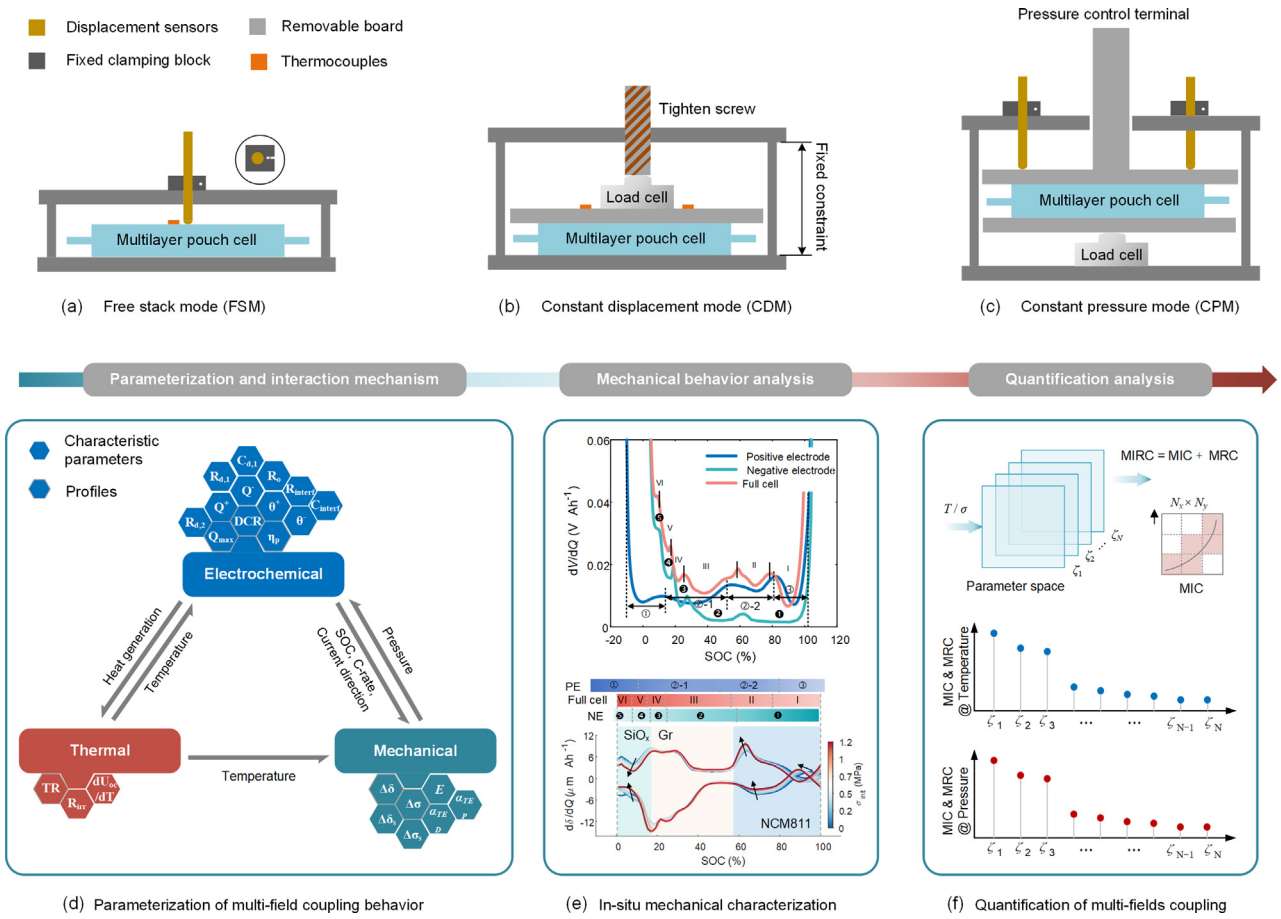

(a) Free stack mode (FSM) (b) Constant displacement mode (CDM) (c) Constant pressure mode (CPM)

(d) Parameterization of multi-field coupling behavior (e) In-situ mechanical characterization (f) Quantification of multi-fields coupling

Fig. 1. Schematic overview of test platforms and in-situ quantitative analytical framework.

Introducing a composite metric for quantitative assessment of multi-field coupling under mechanical constraints, we synthesized nonlinear correlations and coupling intensities between characteristic parameters and physical fields. Our comprehensive approach, combining experimental matrices and non-invasive quantitative analysis, successfully addressed challenges in analyzing strongly coupled problems. This effort significantly deepened our understanding of underlying interaction mechanisms in multi-physics couplings within LIBs, laying a robust theoretical foundation for model development and enhancing BMS reliability.

Table 1
Specifications of the battery cells used in this work.

Specifications	Sample
Cathode materials	NCM811
Anode materials	Gr-SiO_x
Capacity (Ah)	62
Voltage range (V)	2.5–4.2
Temperature (°C)	−20–50
Cell dimension (mm × mm × mm) (Length × width × height)	291 × 100 × 10.96
Maximum chg. /dis. rate (C)	1/1.5
Weight (g)	1005

2. Experimental

2.1. Battery and test platforms

Experiments are performed on commercial LIB pouch cells with voltage ranges from 2.50 to 4.20 V, operating temperature from −20 to 50 °C, and a nominal capacity of 62 Ah. The LIBs are comprised of the cathode of $LiNi_{0.8}Co_{0.1}Mn_{0.1}O_2$ (NCM811) and composite anode of graphite and silicon oxide (Gr-SiO_x). A more detailed description of the battery cells is summarized in Table 1. The sandwich-type electrode layers and z-folded separator configuration allow a less pronounced edge effect and more uniform electrochemical and mechanical performance than a wound jelly roll.

In Fig. 1(a), the FSM structure is depicted for measuring swelling displacement. A high-precision, low-stiffness contact-type displacement sensor (MILONT, G250-50MM-A2, China) with a resolution and accuracy of 0.1 μm was secured on a high-stiffness bench frame using a clamp. The displacement probe was positioned towards the battery center, where the most uniform expansion occurs [28], enabling swelling measurements under FSM. This sensor measures relative displacement from a preset reference value of 2500 μm. Additionally, T-type thermocouples were employed to monitor battery surface temperatures.

Fig. 1(b) illustrates the CDM structure designed for swelling force measurements. This sandwich structure, implying a fully rigid bracing mode with no expansion space, comprises three aluminum alloy plates, a tightening mechanism with a single-axis screw, a locking device with four horizontal screws, two T-type thermocouples, and a piezoelectric pressure sensor. The test bench's equivalent stiffness surpasses that of the target batteries, ensuring battery deformation solely under constrained conditions. By tightening the single-axis screw, we exert pressure on the battery while simultaneously maintaining a fixed initial cell thickness.

The expansion force induced by particle volume change from charging and discharging is transmitted to the load cell through a middle plate. This load cell (SMOWO, LCS-M7 China) has a capacity of 5 t and a resolution of 0.1 kg.

In Fig. 1(c), the swelling of the cell was measured using high-precision pressure (resolution and accuracy of 0.1 kg) and displacement sensors (resolution and accuracy of 0.1 μm) combined with an adaptive pressure regulation control system based on the multiple swelling measurement modes (SWE2110, IEST, China). The in-situ expansion tester simulates CPM constraint conditions within the battery module and allows chamber temperature adjustments. Throughout the experiment, data on expansion force, temperature, voltage, and current signals are collected via corresponding sensors. Fixtures for FSM and CDM are placed within a temperature-controllable chamber (SURUI, RGDJS-500, China) and connected to charge/discharge equipment (Arbin, LBT 5 V-100A, USA) and an electrochemical station (Biologic, VMP-300, France).

2.2. Testing procedure

Given the irreversible effects of mechanical stress on cell chemistry, four cells were used for the following tests. Table 2 presents details of the specific mechanical constraints, cells used, temperature, and pressure ranges within each experiment, along with extracted profiles and relevant parameters derived from these experiments.

Experiment I involved unpressurized cells undergoing charging and discharging at 0.1 and 1 C, repeated at 10, 25, and 40 °C to analyze the impact of temperature on swelling displacement.

Experiment II, performed under CPM, assessed swelling displacement across various initial pressures using pressurized cell during charge and discharge cycles at 0.1 and 1 C. The specific pressure values are listed in Table 3. Due to cost considerations, these tests were exclusively conducted at room temperature.

Experiment III, conducted under CDM, focused on characterizing mechanical-induced electrochemical behavior at 10, 25, and 40 °C. This test involved pressurizing the fully-discharged cell to a target initial pressure value σ_{init}. Note that the following electrochemical tests were performed under external mechanical loads. After a stable period of 5 h to minimize stress relaxation (initial stresses listed in Table 3), the battery underwent charging and discharging phases at a constant current (CC) of 0.05 C between the upper and lower voltage limits, which can be used for the estimation of thermodynamic parameters and elastic modulus. The battery was then charged at a specific current, such as 0.5, 1, and 1 C until reaching the upper voltage limit, followed by a constant voltage (CV) phase until 0.05 C, and discharged at 0.5, 1, and 1.5 C until reaching the lower voltage limits in the first phase, followed by a 1 h rest. The charge currents were less than 1 C due to the maximum charge current limitation. To completely discharge LIBs, a discharge current of 0.05 C follows closely until reaching the lower voltage limits again. Upon discharging the cell to every 10% of maximum capacity, the cell underwent a 1 h rest, followed by a potentiostatic EIS test in a particular bracing mode. The EIS test condition comprised a perturbation voltage of 5 mV over a frequency range from 10 kHz to 10 mHz, with 12 points per decade. Note that the maximum capacity is the average of charge and discharge capacity of 0.05.

Table 3
Detailed information of the experimental datasets under CDM.

Cell No.	Temperature (°C)	Initial pressure (kPa)
1	10	0, 2, 73, 144, 238, 355
2	25	6, 27, 52, 80,179, 320
3	40	2, 10 85, 174, 273, 393
4	25	0, 10, 25, 50, 100, 200, 400, 800, 1200

Experiment IV aimed to evaluate cell thermal-mechanical coupling behavior, specifically thermal expansion pressure under CDM. The cell was charged using a 0.5 C current at 25 °C to reach target SOCs, i.e., 20%, 50%, and 80%. Subsequently, a 6 h relaxation period was implemented to achieve a stable state. Following this, thermal cycle tests were carried out, varying cell temperatures from 5 to 45 °C in 10 °C increments. Simultaneously, multi-sensor signals were acquired to evaluate the temperature effects on thermal expansion behavior. To isolate thermal expansion sorely from the cell, a supplemental experiment involved cycling the fixture and sensor without the cell installation, eliminating external factors influencing cell thermal characterization.

Experiment V involved designing an FSM-based comparison group with and without an air-cooling system, incorporating high-power fans, a heat sink, and thermal-conductive silicon grease to verify the cell thermal swelling during the diffusion process. These experiments are conducted at 1 C charge and 1.5 C discharge at 40 °C because of the limitation of air-cooling capability. A 1 h of relaxation time between charging and discharging ensures that the temperature falls back to 40 °C at the beginning of discharging. The discrepancy observed in temperature and displacement at the charge and discharge endpoints aimed to characterize the thermal swelling during the diffusion process.

3. Methodology

3.1. In-situ quantitative analytical framework

The utilization of LIBs within interdisciplinary applications involves multiple physical fields, including electrochemical, thermal, and mechanical aspects. However, practical engineering challenges often necessitate resolving the interplay among these physical fields, resulting in multi-field coupling problems. Analyzing multi-field problems is notably intricate due to the involvement of diverse disciplines and nonlinear coupling behaviors. In

Table 2
Profiles and relevant parameters from experiments under various mechanical constraints.

No.	Mechanical constraint	Cell number	Pressure (MPa)	Temperature (°C)	Profiles_x	Parameters
I	FSM	1	0	10, 25, 40	$\Delta\delta$_t, DSV_t,	Mechanical: $\Delta\delta_s$_t
II	CPM	4	0–1.2	25	$\Delta\delta$_m, DSV_m	Mechanical:$\Delta\delta_s$_m
III	CDM	1,2,3	0–0.4	10, 25, 40	$\Delta\sigma$_m, DSV_m, TED_c_t	Mechanical: $\Delta\sigma_s$_c, α_{TEP}_t Thermal: R_{irr} Electrochemical: Q_{max}, DCR, η_p, θ^+_c, θ^-_c, Q^+_c, Q^-_c, R_o_c, R_{interf}_c, C_{interf}_c, $R_{d,1}$_c, $C_{d,1}$_c, $R_{d,2}$_c
IV	FSM, CDM	1	0, 0.1	5, 15, 25, 35, 45	TED_c_t, TEP_c_t	Mechanical: α_{TED}_t, α_{TEP}_t
V	FSM	1	0	45	TR, $\Delta\delta$_t	Mechanical: $\Delta\delta_s$_t

Note: x = t, m, and c represent thermal, mechanical, and coupled thermal-mechanical domain.

this study, we propose an in-situ quantitative analytical framework depicted in Fig. 1, aiming to address these complexities comprehensively. Targeting the unmeasured battery temperature under mechanical constraints, we elaborate a comprehensive experimental matrix by combining three mechanical platforms to provide data support for parameterizing multi-field models and analyzing mechanical characteristic profiles. Initially, to quantitatively assess the intricate interplay among different fields, we visualized and parameterized coupling behaviors using equivalent circuit, mechanical, and thermal models that capture the dynamics of LIBs in Fig. 1(d). As shown in Table 2, the characteristic parameters of models and profiles were extracted from different characterization tests to reveal the electrochemical nature of pressure-induced controlling step changes at different temperatures. This provides an important basis for visual quantification of the multi-field coupling between the characteristic parameters and physical fields. While thermal effects on mechanical behavior are explored using a one-way coupling approach, interactions among other physical fields entail a two-way coupling strategy. Subsequently, to further investigate the effects of temperature and pressure on mechanical behavior, we developed an in-situ mechanical characterization method using differential voltage and swelling analysis, as illustrated in Fig. 1(e). This method allows us to explore the electrochemical underpinnings of changes in mechanical behavior by correlating swelling peaks with specific phase transitions. Additionally, we introduced a composite metric that combines the maximum information coefficient (MIC) and maximum change of rate (MRC) to quantitatively assess the coupling correlation and intensity between characteristic parameters and physical fields. This framework, depicted in Fig. 1(f), guides the design of experiments to decouple interactions and the creation of models specifically addressing the challenges of multi-field coupling.

3.2. Equivalent circuit model

Considering the advantage of open circuit voltage (OCV)-based and impedance-based models in decoupling thermodynamic and kinetic parameters within cell dynamics, an equivalent electrochemical model was selected as the basic model in this work, as shown in Fig. 2, which can be represented as follows

$$\mathrm{SOC} = \mathrm{SOC}_0 - \frac{1}{C_{\mathrm{N,t}}}\int_{t_0}^{t} \eta I \mathrm{d}t \tag{1}$$

$$U_t = \mathrm{OCV} - I \cdot Z_{\mathrm{sim}} \tag{2}$$

where I and U_t are the input current and terminal voltage; SOC_0 and SOC are the initial and current state of charge (SOC); $C_{\mathrm{N,t}}$ is normal capacity; η is the Coulomb efficiency and set to be 1 due to greater than 99.9% Coulomb efficiency of commercial batteries; OCV is the open-circuit voltage; and Z_{sim} is an simulated impedance model of

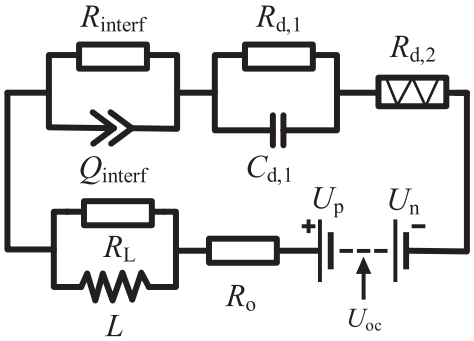

Fig. 2. An equivalent circuit model.

the full-frequency domain. When the frequency is 0.159 Hz, Z_{sim} can be approximated to the direct current resistance (DCR) of 1 s, as reported by Ruan et al. [31]. Polarization voltage η_{p} at the end of discharge is calculated by measured U_{t}, OCV, and estimated DCR according to polarization voltage $\eta_{\mathrm{p}} = U_{\mathrm{t}} - \mathrm{OCV} - I \times \mathrm{DCR}$. To accurately monitor changes in the OCV-SOC curves caused by varying temperatures and pressures, we developed an OCV-reconstruction method that has been integrated into the impedance-based model.

$$\mathrm{OCV} = f_{\mathrm{p}}(\theta^{+}) - f_{\mathrm{n}}(\theta^{-}) \tag{3}$$

$$\theta^{+} = \theta_0^{+} + \mathrm{Q_{cell}}/\mathrm{Q_{max}^{+}} \tag{4}$$

$$\theta^{-} = \theta_0^{-} + \mathrm{Q_{cell}}/\mathrm{Q_{max}^{-}} \tag{5}$$

where θ_0 and Q_{max} represent the initial lithium intercalation site and the electrode capacity; Q_{cell} is the cell's average charge and discharge capacity of 0.05 C under different temperatures and pressures. The superscripts '+' and '–' correspond to positive and negative electrodes. The identification of thermodynamic parameters has been performed using the particle swarm optimization algorithm [47].

To gain insight into the quantitative analysis of pressure-induced electrochemical reactions under varying temperatures, we can observe that the battery impedance across different frequency ranges can be simplified into four parts, namely a low-frequency straight line, a low-frequency semi-circle, a mid-frequency semi-circle, and a high-frequency tail. For an equivalent circuit model, we need to superimpose the impedance of the high-frequency tail representing mainly the cable connection inductance, the semi-circle corresponding to the migration through the passivation film, and the semi-circle indicating the electrochemical reaction. The resulting equivalent circuit model for our assumptions is described by the following Eq. (6).

$$Z_{\mathrm{sim}}(\omega_n) = \frac{R_{\mathrm{L}}}{1 + R_{\mathrm{L}}/(Lj\omega_n)} + R_{\mathrm{o}} + \frac{R_{\mathrm{int}}}{1 + R_{\mathrm{int}}Q_{\mathrm{int}}(j\omega_n)^{\alpha}} + \frac{R_{\mathrm{d,1}}}{1 + R_{\mathrm{d,1}}C_{\mathrm{d,1}}(j\omega_n)} + \frac{R_{\mathrm{d,2}}}{(j\omega_n)^{\beta}} \tag{6}$$

where j is imaginary number; ω_{n} denotes angular frequency; R_{L} and L represent the resistance and inductance of the cables. R_{o} represents the ohmic resistance. R_{int} and Q_{int} stand for the resistance and capacitance at the interface of the solid and liquid phases. $R_{\mathrm{d,1}}$ and $C_{\mathrm{d,1}}$ denote the resistance and capacitance of diffusion processes in the electrolyte. Finally, $R_{\mathrm{d,2}}$ is the resistance of diffusion processes in other particles as well as the inverse of the Warburg coefficient.

To assess the quality of the impedance parameter sets generated during the global optimization process, the fitness functions employed in the process will significantly affect the final identification outcome. This study aims to minimize root-mean-square error (RMSE) between the simulated model impedance Z_{sim} and the measured impedance Z_{exp}, for a given input frequency using the fitness function FF_I given in Eq. (7).

$$FF_I = \sum_{n=1}^{N}\left[\frac{1}{w}\cdot \mathrm{Re}(Z(\omega_n))^2 + w \cdot \mathrm{Im}(Z(\omega_n))^2\right] \tag{7}$$

$$Z(\omega_n) = \log\frac{Z_{\mathrm{sim.}}(\omega_n)}{Z_{\mathrm{exp.}}(\omega_n)}, n = 1, 2, \cdots, N \tag{8}$$

where N represents the number of the data points of the EIS dataset; Re and Im stand for the real and imaginary parts of the impedance $Z(\omega_n)$, respectively. w is the weight factor, which is 0.5 in this paper. The weight selection has a notable impact on the identification results, which can be determined by analyzing the error

terms to ensure that all terms are on the same order of magnitude during optimization.

3.3. Equivalent mechanical model

Given homogeneity, uniaxial expansion, and contraction in the *z*-direction of the cell, a simplified one-dimensional mechanical model was selected as the basic model in this work. Previous studies have confirmed that above homogeneity and negligible lateral contraction are reasonable assumptions [48]. Considering the thermal expansion, according to Hook's law, the diffusion-induced stress-strain relationship [11] is written as

$$\sigma = \frac{F}{A} \tag{9}$$

$$\varepsilon - \alpha(T - T_0) = \frac{\sigma}{E} \tag{10}$$

where ε is the current strain; stress σ is equal to the compression force F divided by the unit area A of the cells; α is the thermal expansion coefficient; T and T_0 are the current and initial temperature; and E is the elastic modulus.

In Eq. (10), quasi-equilibrium thermal expansion pressures (TEP), i.e., $\alpha \times E$, and thermal expansion displacement (TED) are measured in the range from 5 to 45 °C with 10 °C increments. The measured data needs to be calibrated due to the disturbances of the thermal effect of the fixture and sensor. Hence, the cell thermal expansion can be calculated as follows.

$$\mathrm{TEP_c} = \gamma_\mathrm{p} \times (\mathrm{TEP_m} - \mathrm{TEP_f}) \tag{11}$$

where γ_P is the conversion coefficient of the unit from kg to MPa, which is 3.4364×10^{-4} N/(kg mm^2). The subscripts 'c,' 'm', and 'f' denote the swelling pressure of the cell, measured, and fixture.

According to Eq. (10), the second term is neglected when there is no TR during charge or discharge at a low C rate, i.e., 0.1 C. In this case, when stress and strain are proportional, the slope of stress-strain curves is E. However, the $\Delta\sigma/\Delta\delta$-SOC curves are strongly nonlinear. Thus, with the assumption that $\Delta\delta$ remains unchanged with pressure, we can approximate E by the ratio of linear regression slope of stress and strain within the 2% boundary of target SOCs.

$$\varepsilon = \frac{\delta - \delta_0}{\delta_0} = \frac{\Delta\delta}{\delta_0} \tag{12}$$

$$E = \frac{\mathrm{d}\sigma}{\mathrm{dSOC}} = \delta_0 \cdot \frac{\mathrm{d}\sigma/\mathrm{dSOC}}{\mathrm{d}\delta/\mathrm{dSOC}}\Big|_{\Delta\mathrm{SOC}_j} \quad j = \mathrm{l,m,h} \tag{13}$$

where δ_0 is the initial thickness; $\Delta\mathrm{SOC}_j$ is the target SOC, and j = l, m, and h represent 25%, 45%, and 75% SOC, respectively.

The above equation can reveal the effect of pressure on E at different SOC points and initial stresses through linear regress at specific SOC regions, but it cannot analyze the effect of C-rate on E in the whole SOC range due to the nonlinear lithiation expansion. The invariance of the expansion shape and stress-dependent of E indicates that the stress dependence of $\Delta\sigma$ extensively stems from E. To elaborate on the correlation between E and C-rate, we need to establish a stretch model and then hypothesize that E is C-rate dependent if the identified stretch parameters at a certain C-rate possess inferior simulation accuracy at other C-rates. To determine the leading cause of E in $\Delta\sigma$, it is necessary to exclude the effect of C-rate on $\Delta\delta$. Thus, $\Delta\sigma$ of each C-rate under maximum pressure was selected as the benchmark curve. According to the test data of Sateriger et al. [21] and estimated in Eq. (13), E has a double exponential function with σ. As a result, we define a tensile function K, a bi-exponential function with stress in Eq. (14), and nonlinearly stretch the benchmark stress series to the current one by K, as described in Eq. (15).

$$K(\sigma_{i,k}) = \xi_{i,1} \cdot \exp\left(-\xi_{i,2} \cdot \sigma_{i,k}\right) + \xi_{i,3} \cdot \exp\left(-\xi_{i,4} \cdot \sigma_{i,k}\right) \tag{14}$$

$$\hat{\sigma}_{i,k} = \hat{\sigma}_{i,k-1} + K(\sigma_{i,k}) \cdot \beta(SOC_{i,k}) \cdot \left(SOC_{i,k} - SOC_{i,k-1}\right), \quad i = 1,2,\cdots N_\mathrm{a}, k = 1,2,\cdots N_\mathrm{s} \tag{15}$$

where ξ represents the coefficient of the bi-exponential function; β denotes the differential benchmark stress profile; and $\hat{\sigma}_i$ reflects the current stress sequence under initial stress $\sigma_{i,0}$. N_s is the number of current stress curves; N_a is the number of stress series. To reduce the computational burden of the model without sacrificing accuracy, we sparse all stress series to within 50 points. This study aims to minimize RMSE between the simulated model stress, $Z_\mathrm{sim.}$, and measured stress, $Z_\mathrm{exp.}$, for a given SOC input using the fitness function FF_σ.

$$FF_\sigma = \sqrt{\frac{1}{N_\mathrm{s}} \sum_{k=1}^{N_\mathrm{s}} \left(\sigma_{i,k} - \hat{\sigma}_{i,k}\right)^2}, \quad k = 1,2,\cdots N_\mathrm{s} \tag{16}$$

Additionally, the maximum swelling stroke, $\Delta\delta_\mathrm{s}$ and $\Delta\sigma_\mathrm{s}$, in Eq. (17) are selected as two parameters to characterize the swelling behavior of the cell under various mechanical constraints.

$$\begin{cases} \Delta\sigma_s = \sigma_\mathrm{max} - \sigma_\mathrm{min} \\ \Delta\delta_s = \delta_\mathrm{max} - \delta_\mathrm{min} \end{cases} \tag{17}$$

The subscript 'max' and 'min' denote the maximum and minimum swelling values.

3.4. Equivalent thermal model

In the Bernadi equation, the total heat generation rate can be described as follows if we neglect the heat from mixing, phase changing, and the heat-storing effect [7].

$$\dot{Q} = I^2 R_\mathrm{irr} - IT\left(\frac{\mathrm{d}U_\mathrm{oc}}{\mathrm{d}T}\right) \tag{18}$$

The first term is the irreversible heat generation rate. R_irr is the corresponding thermal resistance that causes the terminal voltage drop, which includes R_L, R_o from contact resistance, electronic and ionic conduction, R_interf, as well as total R_d from ion diffusion inside electrolyte and active particles. The second term is the reversible heat generation rate, and $\mathrm{d}U_\mathrm{oc}/\mathrm{d}T$ is the entropy coefficient of the cells. The non-significant effect of pressure on $\mathrm{d}U_\mathrm{oc}$ /$\mathrm{d}T$ has been reported by Du et al. [7] and will not be further discussed in this work. In addition, R_irr can be calculated by the real impedance at 10 mHz to cover the total resistance due to minute-level continuous heat generation. The selected SOCs are 20%, 50%, and 90% in this work.

3.5. In-situ mechanical characterization

To investigate the electrochemical nature of the mechanical behavior, we perform the differential analysis of the swelling and potential curves to clarify the relationship between the electrochemical phase transition and the crystal structure. By combining the differential voltage peaks from cell balancing, we can decipher the dominant phase transition processes that cause volume expansion and contraction. These processes are reflected in the voltage, expansion displacement, and stress characteristic peaks of the full cell. The differential peaks can be described as follows.

$$\mathrm{DXQ} = \mathrm{d}X/\mathrm{dQ}, \quad X = \mathrm{S,V} \tag{19}$$

where S and V represent swelling, including δ, σ, and voltage data. To obtain undistorted DSQ curves, we use spline interpolation with a capacity width of 0.2 Ah and a smooth filter with a sliding window of 200 for the differential swelling curve at 0.1 C. For higher C-rate

expansion curves, the interpolated capacity and sliding window width are less than 0.1 Ah and 20 to ensure that processed data do not lose vital information. A voltage width of 5 mV and a smooth filter with a sliding window of 10 were selected for differential voltage versus capacity (DVQ) curves.

3.6. Quantifying assessment of multi-field coupling behavior

To quantitatively assess multi-field coupling behavior, we proposed a composite metric of the nonlinear correlation and rate of change between the model parameters and the external factors. The metric, called MIRC, is the sum of MIC and MRC between the model parameters and physical fields in Eq. (20). The former is a statistical measure of the strength of the nonlinear association between two-variable relationships that can capture a wide range of functional and non-functional relationships between variables [49]. The MIC of measuring dependence should have two heuristic properties: generality and equitability. The latter is a measure of the degree of change in the model parameters affected by the operating environment.

$$\mathrm{MIRC} = \mathrm{MIC} + \mathrm{MRC} \tag{20}$$

By generality, the MIC with sufficient sample size can capture a wide range of interesting associations that are not limited to specific functional types. By equitability, it should give similar scores to equally noisy relationships of different types [50]. Intuitively, MIC is based on maximal information-based nonparametric exploration statistics for identifying and classifying relationships by exploring a maximum grid resolution of partitioning the scatterplot of the two variables. The mutual information (MI) of the random variables X and Y is defined as the relative entropy of their joint distribution $p(x, y)$ and their marginal distributions $p(x)$ and $p(y)$ according to Eq. (21). The scatter plot of these variables is partitioned by the grid G of N_x-by-N_y so that the frequency of data points in the (x, y)-th grid is utilized to estimate the joint and marginal distributions.

$$I(X;Y) = \sum_{i=1}^{N_x}\sum_{j=1}^{N_y} p(x_i, y_j)\log\frac{p(x_i, y_j)}{p(x_i)p(y_j)} \tag{21}$$

where x_i and y_j belong to the dataset of the (i, j)-th grid for the random variables X and Y. N_x and N_y refer to the number of grids partitioned in the x- and y-direction, respectively. The maximum MI can be calculated by adjusting the split points of the x and y axis for a grid with N_x-by-N_y resolution. As the fact of $0 \le I(X;Y) \le \log(\min(N_x, Ny)$ [49,50], the grid resolution that maximizes the normalized MI is utilized as the MIC metric.

$$\mathrm{MIC}(X;Y) = \frac{\max\limits_{N_x \cdot N_y < B}(I(X;Y))}{\log(\min(N_x, N_y))} \tag{22}$$

where the resolution of the network is restricted to $N_x \times N_y < B$ by any x-by-y grid applied to the data, B is a function of the sample size, and we generally set $B = n^{0.6}$ with n being the length of the two-dimensional finite set.

To satisfy the generality and equitability of MIC, we utilize statistical data of parameters at varying conditions.

-Three SOCs, 20%, 50%, and 90%, to determine electrochemical and thermal parameters and E;

-Four C-rates, i.e., 0.1, 0.5, 1, and 1.5 C, to determine the remaining mechanical parameters and calculate MIC of a certain stress as follows.

$$Y@\mathrm{MIC} = \sum_{i=1}^{N_c}\frac{\mathrm{MIC}_i}{N_c} \tag{23}$$

where Y represents Temp or Pres, i.e., the abbreviation of temperature and pressure. N_c is the number of conditions, 3 SOC and 4 C-rate conditions.

To compensate for the shortcomings of MIC in evaluating the change rate of model parameters, the normalized MRC can be written as follows.

$$\begin{cases} \Delta\zeta_{\max} = \max\left(\frac{\zeta_i(E_h)-\zeta_i(E_l)}{\zeta_i(E_l)}\right), \quad i = 1, 2, \cdots, N_p \\ Y@\mathrm{MRC} = \frac{\zeta_i(E_h)-\zeta_i(E_l)}{\zeta_i(E_l)\cdot\Delta\zeta_{\max}} \end{cases} \tag{24}$$

where ζ denotes model parameters; N_p is the number of model parameters; E_l and E_h represent low and high boundaries under a certain condition, which are 10 and 40 °C for the temperatures as well as 0 and 0.4 MPa for the pressures. $\Delta\zeta_{\max}$ denotes the maximum change rate of all parameters.

4. Results and discussion

4.1. Pressure effects on electrochemical behavior under various temperatures

To analyze the effect of pressure on electrochemical behavior under varying temperatures, we displaced the evolution of battery performance parameters with pressure, such as DCR, R_{irr}, η_{max} and $\Delta Q/Q_0$ in Fig. 3. In Fig. 3(a), a layered 3D map clearly shows that temperature has a far greater effect on the impedance than pressure. Fig. 3(b–d) demonstrates the changes in DCR with pressure at 10, 25, and 40 °C, respectively. The chosen SOCs are 20%, 50%, and 90% at each temperature. At 10 °C, a strong decrease in DCR with increasing pressure can be observed up to 240 kPa. For higher pressures up to the maximum tested pressure around 500 kPa the DCR does not change significantly. For 25 °C we can observe a nearly linear decrease in DCR from 0 kPa to the maximum tested pressure around 400 kPa. Additionally, the decrease in DCR from the lowest to the highest pressure tested is much less prominent at 25 °C (12.2% decrease) than at 10 °C (44.8% decrease). This phenomenon is attributed to the increased temperature, which increases the contact area between the electrode layer and the current collectors, similar to pressure, reducing the impact of pressure on the DCR. Conversely, the calculated DCR at 40 °C exhibits an increase of 6.3% with increasing pressure, which implies the narrower pathways of the separator and blocked ion diffusion paths with pressure and no compressible gaps between the electrode layer and current collectors and particles at 40 °C. A similar trend was observed for polarization and heat generation change in DCR, as shown in Fig. 3(e and g). This denotes a reduced total diffusion and thermal impedance with increasing pressure. For 40 °C, R_{irr} is only slightly increasing with increasing pressure in Fig. 3(h). This suggests that in our tested ranges, pressure change has much less effect on the heat generation rate than temperature variation. The change in impedance further results in changes in irreversible heat generation. η_{max} decreases with pressure, except for 40 °C, which is attributed to the reduction of DCR and R_d at 10 and 25 °C, while increasing DCR and diffusion impedance at 40 °C. The reasons for enhanced DCR at 40 °C have been discussed in the previous description. However, η_{max} exhibits a greater change at 10 °C than that at other temperatures, with consistent results across various current rates. Thus, in Fig. 3(f), the reduction of 1.5 C capacity at 25 and 40 °C is mainly caused by decreasing maximum electrode capacity, while the higher 1.5 C capacity at 10 °C (maximum 7.81% at 240 MPa) is attributed to the lowered DCR and diffusion impedance. The conclusions are further verified by the change in electrode capacity and diffusion resistance with pressure, as shown in Fig. 4(f, k and l).

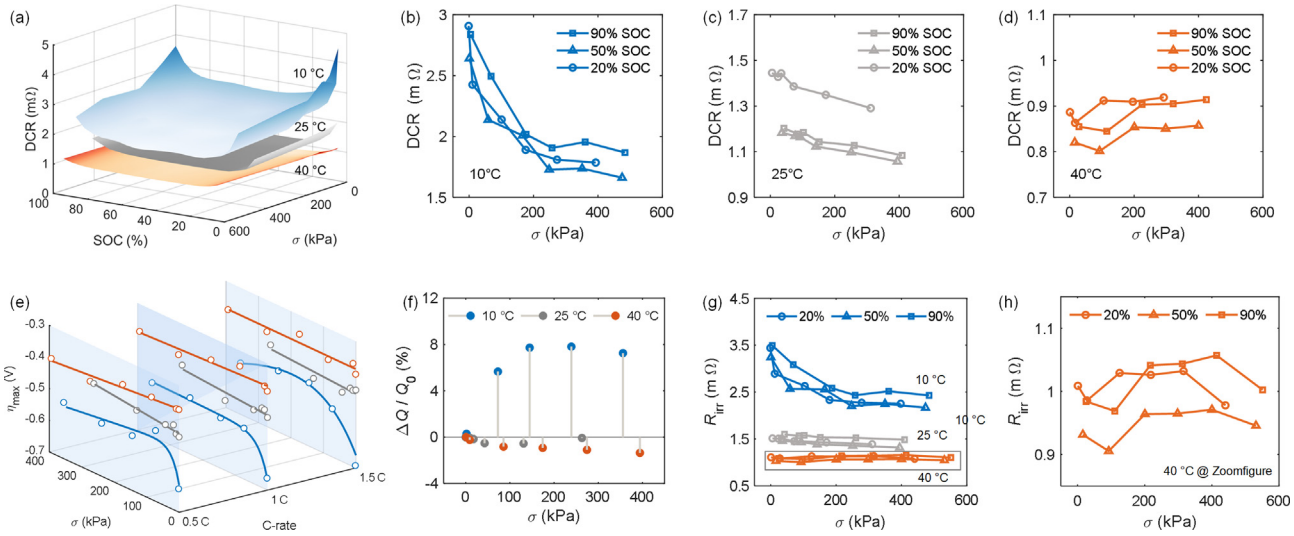

Fig. 3. Pressure-induced cell performance change under various temperatures. (a) 3D map plot of SOC, σ_{init}, and DCR. The change in DCR with initial stresses at (b) 10 °C, (c) 25 °C, and (d) 40 °C. (e) Pressure effect on polarization voltage at varying C-rates and temperatures. (f) Pressure effect on discharge capacity at 0.1 C. (g) Pressure-induced thermal resistance and (h) zoom figure at 40 °C.

To further reveal the internal electrochemical mechanism of battery external performance change, the evolution of cell thermodynamic and kinetic parameters with increasing pressure under different temperatures was shown in Fig. 4. Fig. 4(b) shows the Nyquist plot of EIS at 10 °C, revealing the effect of pressure on the ohmic effect in the high-frequency range, middle-frequency interfacial reaction, and low-frequency diffusion processes. R_o is the combination effect of electrical impedance R_{el} in the solid phase and ionic impedance R_{ion} in the liquid phase. As illustrated in Fig. 4(c), R_o decreases with stress under all temperatures except for 40 °C. Such an observance was explained by the dominance of the electrical contact state affected by external stress under low temperature, while ionic impedance was dominant under high temperature. The R_{ion} of the electrode increases with the increment in stress [6] for both electrodes, while R_{ion} of the separator may decrease in some cases [51]. The thermal expansion of active mate-

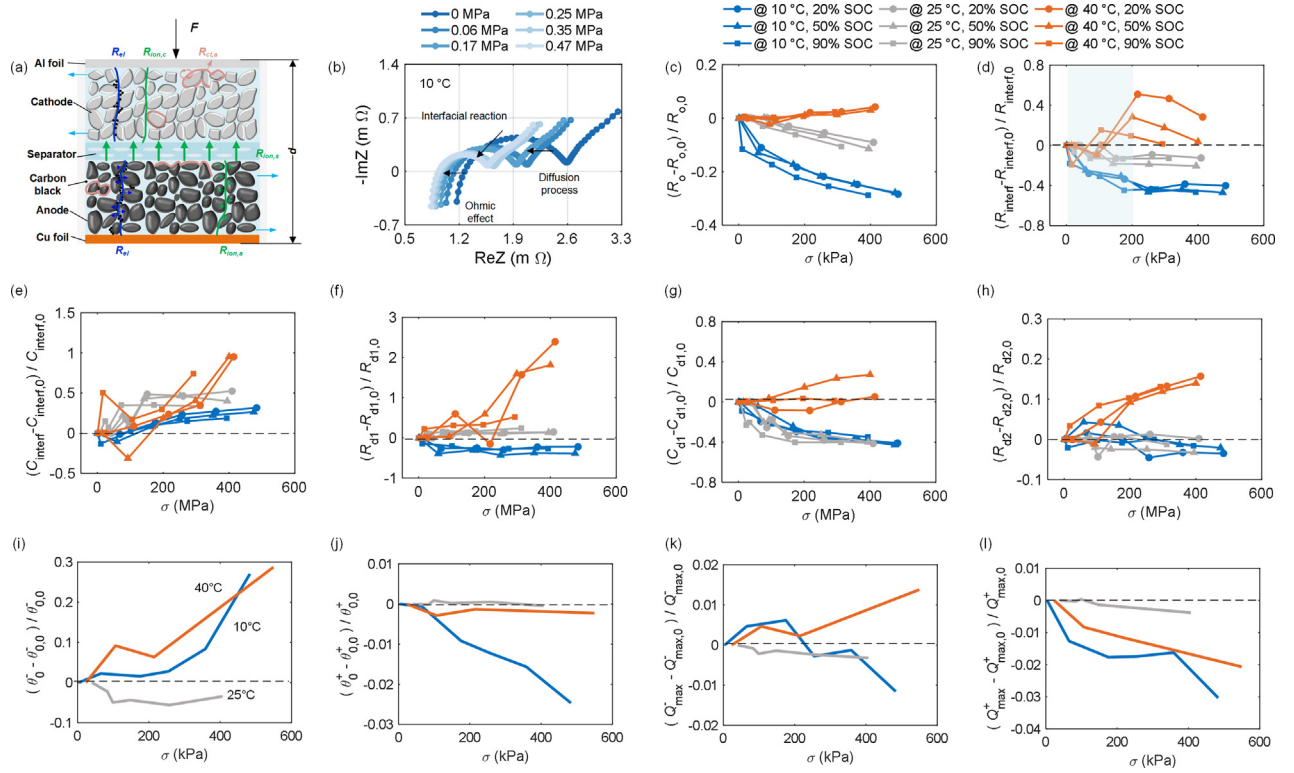

Fig. 4. (a) Nyquist plot of EIS. (b) Schematic diagram of the effect of pressure on electrochemical properties. The resistance from the initial value (R_0) under low stack stress is calculated from comparison. (c) Ohmic resistance. (d) Interfacial resistance. (e) Interfacial capacitance. (f) Electrolyte diffusion resistance and (g) capacitance. (h) Other diffusion resistance. The stress-induced thermodynamic parameters. Thermodynamic parameters include the initial lithiation state of (i) anode and (j) cathode. (k) Anode and (l) cathode capacity.

rial particles facilitates the tightening of connections among particles, binders, and conductive materials. This results in R_{el} remaining constant with increasing pressure due to the absence of voids. In contrast, these loosely connected particles at 10 °C lead to a reduction in R_{el} with stress due to the eliminated vacuums. In this case, the change in R_{el} induced by stress is significantly greater than R_{ion}, suggesting that pressurized cells at 10 °C enhance the contact state between each component. However, the extent to which the ionic porosity of a single component is affected by pressure requires further symmetrical cell experiments, like the work of Müller et al. [6]. In Fig. 4(d and e), a decrease in R_{interf} and an increase in C_{interf} were observed with pressure at all temperatures. This suggests that the surface area of the active material particles increases with applied pressure [52] but declines beyond 100 kPa at 40 °C while less than 50 kPa at 20% SOC due to the reduced surface area of AMP caused by mechanical damage, such as embedded particles into the current collector or secondary particle fusion [53]. Therefore, the optimal pressures for maximizing the active surface area, i.e., minimizing the interfacial impedance, are concentrated in the range of 50 to 100 kPa at 40 °C, 100 kPa at 25 °C, and 240 kPa at 10 °C considering the overall SOC range, which provides a powerful theoretical basis for the longevity operation of bracing cells by buffer layers. In Fig. 4(f–h), low-frequency impedances consist of ionic diffusion inside the electrolyte and active particles. $R_{d,1}$ increases with stress at 25 and 40 °C due to reduced porosity while decreases at 10 °C. The results were attributed to the correlation between the diffusion coefficient at 10 °C and stress-induced electrolyte viscosity or even solidification by the Stokes-Einstein equation [54], implying the prominent pressure effect on battery impedance performance at low temperatures. Liquid phase diffusion is the key controlling step in low-temperature performance [55], contributing to improving kinetics by applying external pressure. According to cell electrochemistry, the variation of the control step for the electrochemical reaction can effectively account for the different effects among different temperatures. Although Fang et al. [56,57] reported that the contact stress between particles weakens the stress-induced semicircular arc, the factors affecting the liquid-phase diffusion process are not limited to the contact stress, electrolyte viscosity, and porosity, the dominant factors of which are the key determinants of the change in liquid phases diffusion impedance.

4.2. In-situ mechanical behavior analysis

4.2.1. Thickness change originating from phase transitions

In Fig. 5(a), DVQ curves of cathode and anode materials after OCV matching are plotted to identify each electrode electrochemical contribution in the full cell. According to DVQ profiles, the main contribution processes of differential valleys in the full-cell can be marked as solid '❶' for the anode and hollow '①' for the cathode. In Fig. 5(a), the SiO_x-Gr shows a mixed behavior with three peaks between 0.07 and 0.25 V corresponding to phase transitions in graphite and two peaks around 0.18 and 0.34 V corresponding to amorphous and crystallized phase de-lithiation in SiO_x, i.e., a-Li_xSi and c-$Li_{15}Si_{14}$. In Fig. S1(a), since silicon is the only electrochemically active component in SiO_x, SiO_x and Si anodes show similar peak locations that are 0.08 and 0.24 V on lithiation and 0.29 and 0.46 V on de-lithiation. Obviously, the electrochemical behavior contributed by Gr and Si in the composite anode can be distinguished from the discharge differential voltage (DV) curves of pure graphite and Si in the zoom figure of Fig. 5(b). According to Loudi et al. [39] and Pegel et al. [40], most of the capacity of graphite are released before silicon starts de-lithiation during discharge, which prove that the SiO_x-related electrochemical reactions play a dominant role in the low lithiation state. Another evidence derives from the shape and number of valleys of the DV curve with or without SiO_x in Fig. S1(b), indicating that ❹ ❺DV valleys in Fig. 6(a) come from SiO_x-related electrochemical reactions.

To further investigate the correlation between the involved phase transitions and thickness change, we label the dominant phase transitions of the electrode in asymptotic strips of Fig. 6(a) and plot a combined figure with voltage and thickness change of the electrode from the literature [40], as well as $\Delta\delta$ and $\Delta\sigma$-SOC profiles in Fig. 6(c). It is worth noting that there is a negligible expansion of SiO_x-Gr below 20% SOC, as marked in Fig. 6(b) in the green line. It was attributed to the carbon black-binder-gap around SiO_x particles inside the SiO_x-Gr composite anode [58]. As the previous separable SiO_x-related phase transitions during the lithiation process, we infer that the constant slope of thickness change in the charging SOC range from 20% to 35% originates from the conversion of LiC_{12} to LiC_6 for pure Gr (❸ peak). With validation by thickness expansion comparison between NCM532/Gr and NCM811/Gr-SiO_x cells from Figs. S2 and S3, the results indicate that the slop of thickness change for full cell, 3.57 μm/%, is contributed by Gr anode due to less than 1% thickness change of NCM532 cathode [39], which is close to 4.85 μm/% for SiO_x-Gr during the charging process. Nevertheless, unlike graphite with a fair symmetric expansion profile [37], silicon expands with a highly nonlinear asymmetrical function due to the hysteresis voltage effect and different crystallographic paths during lithiation and de-lithiation. In the discharging SOC range from 20% to 45%, a 6.91 μm/% slope of thickness change for SiO_x-Gr during the discharge is larger than that during charging, as described in Fig. S3. A similar relationship was observed in the swelling over SOC of full cells, which was attributed to the conversion of ❸peak from a-$Li_{15}S_4$ to c-$Li_{15}S_4$. An expansion plateau of Gr facilitates our qualitative analysis of the extent to which silicon is involved during the discharging. As marked in Fig. 6(b) in light blue and green, there is almost no thickness change contribution of NCM811 and about 6% thickness contribution of Gr-SiO_x below 60% SOC. In the SOC range from 0 to 60%, the volume expansion of graphite undergoes a plateau resulting from a phase transformation from x = 0.3 and x = 0.5 in Li_xC_6, that is the right part of ❷peak of the anode, where almost no volume expansion occurs since this transition does not involve lithium intercalating into any empty interstitial layers [40]. The thickness plateau of SiO_x-Gr in agreement with Gr indicates that the asymmetrical expansion and contraction of SiO_x has not yet involved the expansion plateau of the transition phase from Stage 2 to 2L, and hence, SiO_x has finished de-lithiation before entering this phase. In Fig. 6(c), the asymmetry of the expansion properties is more pronounced in $\Delta\sigma_s$ curve due to the different reaction processes forming ❸peak.

Another notable feature emerges in the SOC range from 60% to 100% SOC, where the height of the cell abruptly contracts. Since full lithiation of SiO_x anode has been verified in previous discussions, this phenomenon is ascribed to the combined effect of NCM811 cathode and Gr anode. For Gr, x being lower than 0.3 in Li_xC_6, the cell thickness exhibits a constant slope that suggests a continuous insertion process from graphite to LiC_{18} and reaches a homogenous distribution of LiC_{18} at 33.3% anode SOC (❶ peak). For NCM811, the abrupt contraction of thickness is attributed to the phase transitions from H_2 to H_3 (③ peak), where the S-shape curve of potential and height change vs. specific capacity gets steeper with increasing Ni-content of layered cathode materials [36]. Increasing the Ni-content also results in greater structural instability at high voltage regions, a more significantly reduced c-axis of the rhombohedral crystal structure during de-lithiation, and enormous volume change [59]. As a result, in-situ mechanical characterization helps to analyze thoroughly the differences in E and thermal expansion at different SOCs in subsequent sections, which explains the hysteresis effect of E at 25% SOC (ΔSOC_1 in Fig. 6c) in the later sections.

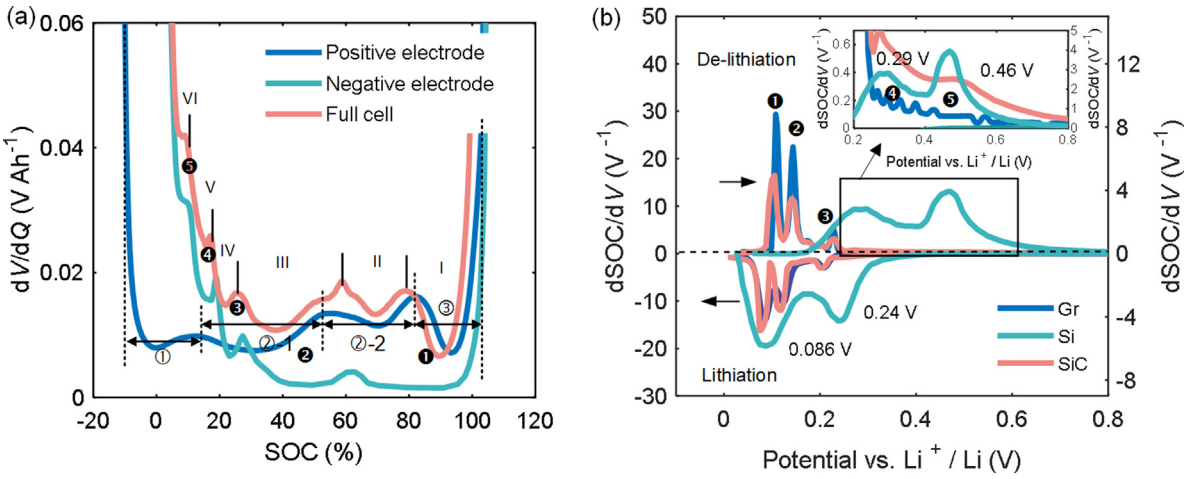

Fig. 5. (a) The domination phase diagram by differential voltage profile and cell balancing. (b) Incremental state of charge analysis of pure graphite, silicon, and composite anode during lithiation/de-lithiation.

4.2.2. Thermal and mechanical effect on cell expansion

Fig. 7(a and b) shows the change in pressure-induced $\Delta\delta$ and $\Delta\sigma$ at 25 °C. Comparing Fig. 7(a and b), some conclusions were discovered that the effect of pressure on $\Delta\sigma$ is more significant than on $\Delta\delta$. Moreover, the asymmetry of $\Delta\sigma$ during charging and discharge is also greater than that of $\Delta\delta$. These findings are attributed to the pressure dependence and asymmetry of E. In Fig. 7(e), increasing peaks of differential pressure versus capacity (DPQ) with stress further proves the above conclusions. The invariance of the pressure-induced swelling shape not only indicates that pressure does not affect the types of host structural transformations rather than their degrees but also provides a basis for elucidating the C-rate dependence of E by a nonlinear stretch model. Although there are only slight changes in $\Delta\delta$ under various pressures and temperatures in Fig. 7(a, c and f), it is essential to understand the influencing factors of swelling to optimize the bracing structural design. According to the in-situ mechanical characterization in Section 4.2.1, differential displacement versus capacity (DDQ) peaks of the full cell has been marked by the symbols of the corresponding phase transitions. This allows us to assign the thermal and mechanical influences on $\Delta\delta$ to the leading phase transitions of a single electrode. In Fig. 7(b), the phase transition reactions affected by pressure are mainly from ❹and ❺peaks for SiO_x, as well as ②-2 and ③peak for NCM811. These peaks all decrease with decreasing pressure, which is the main reason for the decrease of $\Delta\delta_s$ with pressure in Fig. S4(b). Fig. 7(c and f) shows the evolution of the swelling and DDQ curves during the discharge and charge periods at 0.1 and 1 C, respectively. A similar trend in the swelling and DDQ curves of 0.1 C was observed at varying temperatures, except for increasing local maxima or minima values, i.e., ❸peaks for Gr and ③peak for NCM811. The reduction of the co-existence phases at 1 C leads to a larger $\Delta\delta_s$ than 0.1 C and a more significant thermal expansion throughout the SOC range. This behavior can be explained by the fact that the intensity of current alters the ratio of the different fractions of carbon atoms occupied with micro-structure [60], i.e., LiC_6 and LiC_{36}. Thus, pressure mainly impacts the expansion of ❹and ❺peaks for SiO_x and ②-2 and ③peak for NCM811, while temperature primarily affects the expansion of ❸peaks for Gr and ③peak for NCM811. As the C-rate increases, the gradual disappearing transition phase leads to swelling throughout the SOC, suggesting that the expansion under different temperatures may be impacted by the polarization state.

4.2.3. Influencing factors analysis of elastic modulus

To assess the influencing factors of E, Fig. 8 shows the relationship among pressure, temperature, and E during the charge and discharge processes. E increases exponentially with stress under all conditions. The identical relationship at different SOCs is inves-

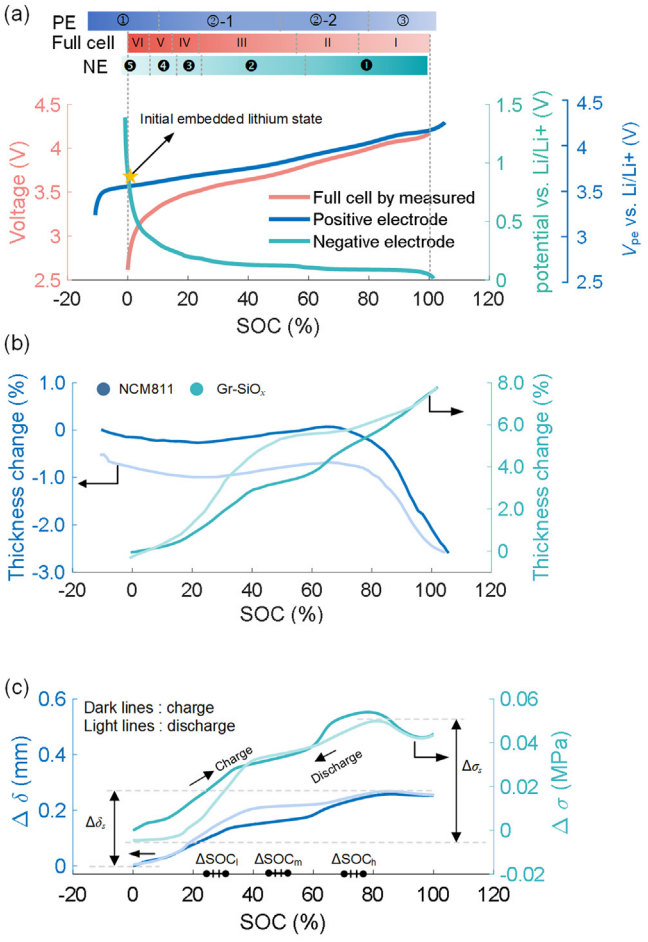

Fig. 6. Thickness change originating from phase transition. (a) Host phase diagram and differential voltage profile after OCV matching. (b) Thickness change of cathode and anode [40]. (c) Swelling displacement and force during charge and discharge.

tigated in Fig. 8(a). The selected SOCs correspond to three respective phases of mechanical behavior in Fig. 5(c). An interesting phenomenon is that *E* for discharge is larger than charge, except for 25%. Apparently, the hysteresis effect of *E* at 25% SOC is more pronounced at 45% and 75% SOC, which can be explained by the different stiffness of the host phase transitions during lithiation/delithiation. As far as we know, the hysteresis effect of *E* is investigated for the first time. *E* at 25% SOC is 0.8 times larger than that

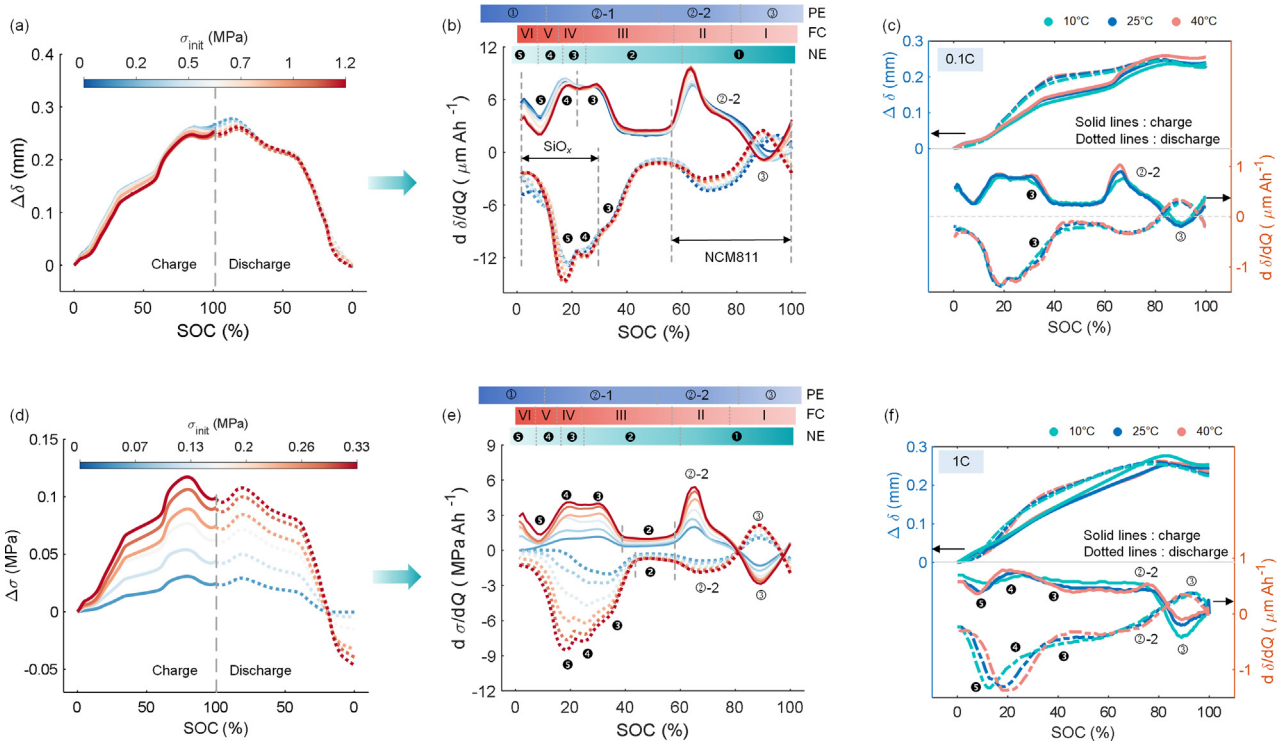

Fig. 7. (a) Expansion displacement and (d) force of 0.1 C charge and discharge at 25 °C when appling various pressures. (b) DDQ and (e) DPQ profiles from (a) and (d). Volume expansion and DSQ curves of (c) 0.1 C and (f) 1 C at 10, 25, 40 °C.

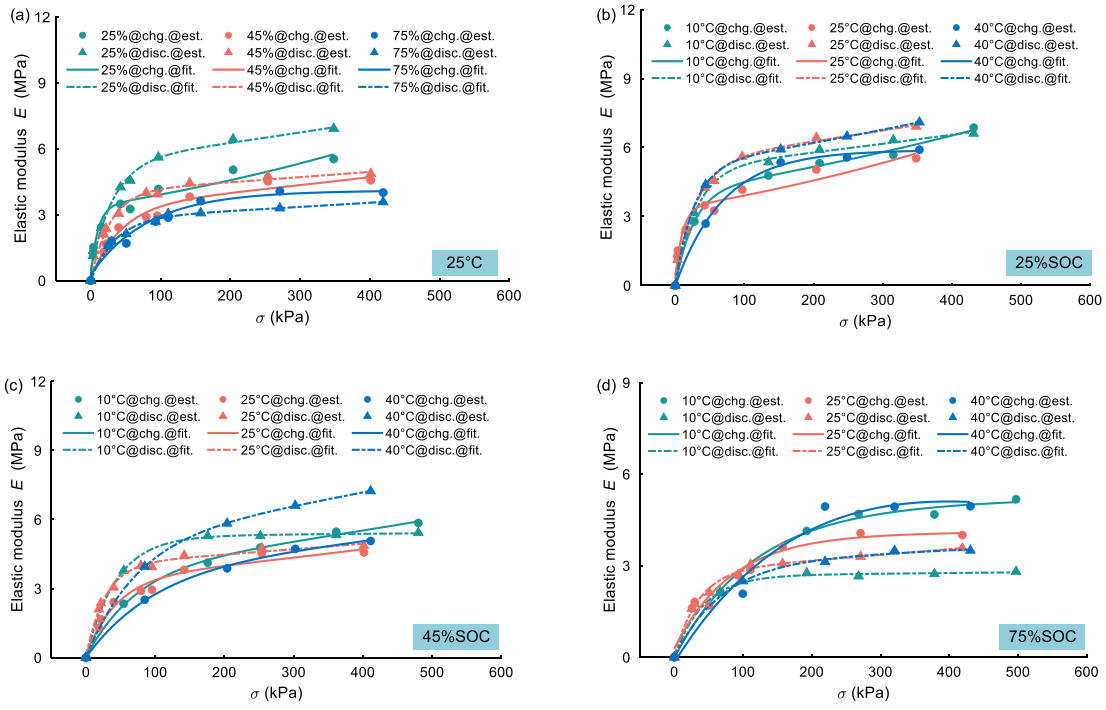

Fig. 8. (a) SOC dependence of *E* with stress under 25 °C and temperature dependence of *E* with stress at (b) 25% SOC, (c) 45% SOC, and (d) 75% SOC.

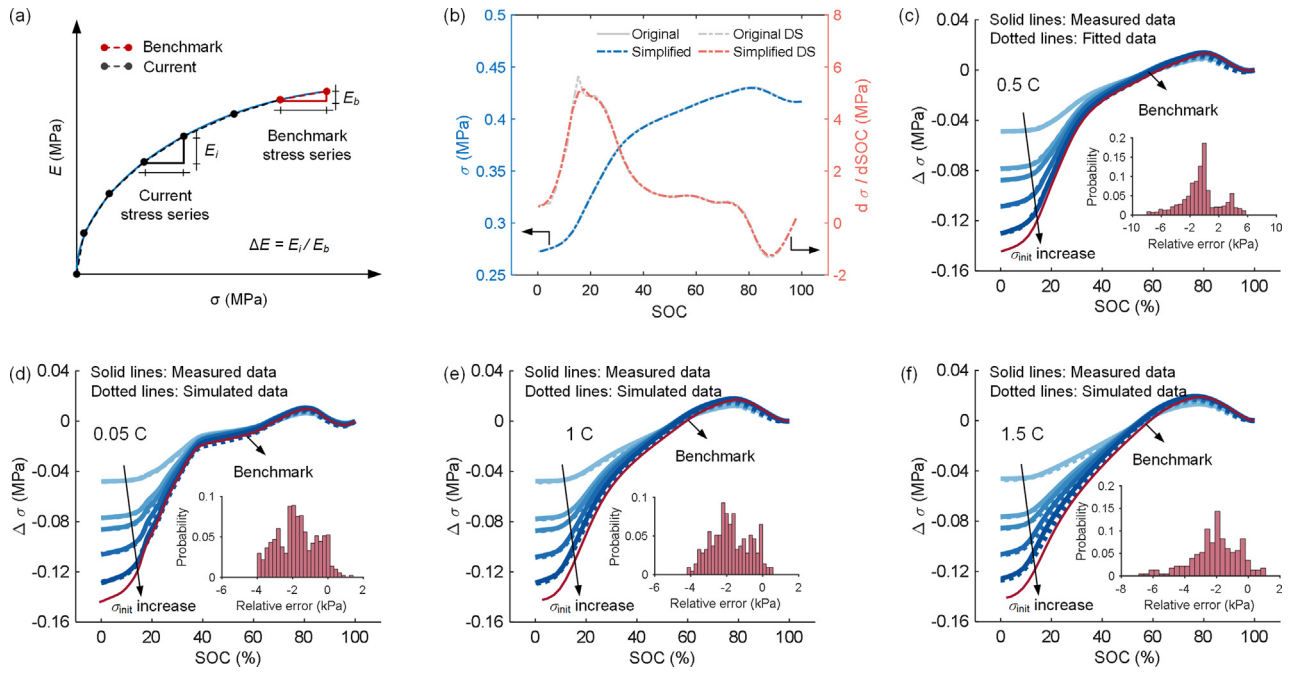

Fig. 9. Influencing factors analysis of elastic module. (a) The relationship of stress and elastic modulus. (b) Original benchmark and differential swelling curve and simplified ones. (c) The results of model parameters identification at 0.5 C discharge and verification results at (d) 0.05 C, (e) 1 C, and (f) 1.5 C discharge of 25 °C.

Table 4
Initial pressure values under different temperatures.

Temperature (°C)	C-rate (C)	Data types	RMSE (kPa)
10	0.5 C	Training	9.79
	0.1 C	Validation	12.08
	1 C	Validation	18.90
	1.5 C	Validation	37.81
25	0.5 C	Training	8.87
	0.1 C	Validation	6.92
	1 C	Validation	12.31
	1.5 C	Validation	12.38
40	0.5 C	Training	12.70
	0.1 C	Validation	8.40
	1 C	Validation	13.54
	1.5 C	Validation	15.31

at other SOCs, indicating a hexagonal α-$NaFeO_2$ structure of NCM811 cathode is softer than LiC_6 of anode. Such a large hysteresis should not be ignored for the battery stress-strain model. Nonetheless, *E* at 25% SOC exhibits a more significant hysteresis effect and lower stiffness than other SOCs. This behavior further proves the cell stiffness with respect to lithiation as well. Additionally, temperature has a relatively weak effect on *E*, as shown in Fig. 8(b–d). Temperature does not show a clear regularity on *E*, which is attributed to the low robustness of the proposed estimation method for weak influencing factors. Hence, the influencing intensity of multiple factors on *E* is ordered as stress > SOC > hysteresis > temperature.

To expedite the parameters identification procedure without sacrificing accuracy, the differential swelling versus voltage (DSV) curve, after smooth filtering and simplification, can effectively reduce the noise of the original benchmark curve and restore its original profile, as sketched in Fig. 9(b). In Fig. 9(c–f), the benchmark curves are colored in dark red, while the solid and dotted gradient blue curves represent the measured and fitted or simulated curves, respectively. As displayed in Fig. 9(c), the nonlinear stretching transformation parameters of different initial stress from the benchmark curve are identified at 0.5 C discharge. The relative error distribution of the measured and fitted expansion curves can be counted from −10 to 6 kPa, indicating the effectiveness of the proposed model and its high fitting accuracy. The maximum relative error of the measured and fitted curves is less than 6.25%. The identified transformation parameters at 0.5 C can serve as inputs for the equivalent model, whereas the stress series represents the corresponding outputs. To evaluate the simulation accuracy of the model, the distribution of relative error is shown in the zoom figure of Fig. 9(d–f) and RMSEs are counted in Table 4. The simulated results are strongly consistent with the measured expansion stress curve. Their relative errors at varying C-rates of 25 °C spread over a range from –8 to 2 kPa. RMSE between simulated and measured data at all temperatures is less than 37.81 kPa. Such high simulation accuracy further proves C-rate independent of *E*.

4.2.4. Analysis of thermal effect on cell expansion

The linear correlation of TEP_f and TED_f with temperature is displayed in Fig. 10(a). The slope of TEP_f and TED_f, i.e., the thermal expansion coefficient of the fixture and sensor, is 0.159 kg/°C and 0.021 μm/°C, respectively. After the above calibrating, TEP_c shows a linear correlation with temperature in Fig. 10(b) and α_{TEP} increases with SOC and ranges from 0.70 to 0.87 kPa/°C. Mathematical analysis of TEP at various SOCs is listed in Table 5. At all SOCs, the fitting error is less than 0.43 kPa, and the adjust-goodness of fit is close to 1. To analyze the magnitude of thermal expansion stresses, we proposed a novel parameter λ_{TEP} to represent the ratio of α_{TEP} and $\Delta\sigma_s$ at 25 °C. The change in λ_{TEP} of less than 2% indicates that TR of 10 °C would lead to a pressure change of less than 20%. Thus, the linear TEP_c was conjectured to be attributed to the temperature dependence of TED_c and *E*. In the zoom figure of Fig. 10(b), the almost invariant TED_c indicates the temperature-independence in the range from 5 to 25 °C while a linear correlation in the range from 25 to 45 °C. A similar positive

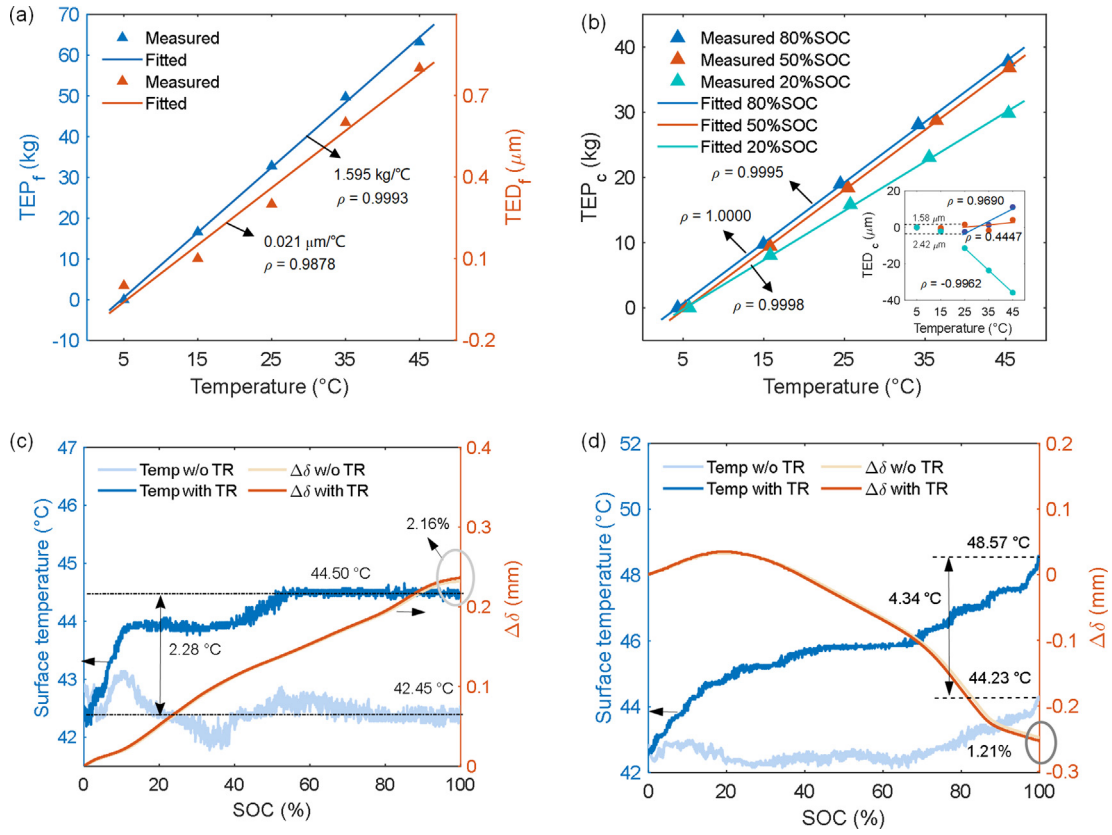

Fig. 10. Thermal expansion characteristic analysis. (a) Thermal expansion pressure of the combined fixture and sensors. (b) Cell thermal swelling pressure and displacement at 20%, 50%, and 80% SOC. The change of temperature and swelling thickness with and w/o TR at (c) 1 C charge and (d) 1.5 C discharge.

Table 5
Mathematical analysis of cell temperature and expansion stress at different SOCs.

SOC (%)	Function	Goodness of fit		α_{TEP} (kPa/°C)	λ_{TEP} (%/°C)
		Adjust-R^2	RMSE (kPa)		
20	$TEP_m = 0.7553\ T - 3.998$	0.9987	0.4290	0.7003	1.2850
50	$TEP_m = 0.9211\ T - 4.943$	0.9999	0.1650	0.8661	1.5892
80	$TEP_m = 0.9274\ T - 3.938$	0.9995	0.3168	0.8724	1.6008

correlation over temperature was observed, except for 20% SOC. The thermal contraction at 20% SOC is attributed to the SiO_x-dominated mechanical properties. This result suggests that cell thermal expansion linearly increases or decreases with temperature after these gaps between electrode layers are filled above 25 °C [8]. However, an opposite trend from TED_c and TEP_c was observed at 20% SOC, indicating that mechanical constraints may result in different experimental results due to differences in contact states between electrodes. Therefore, the above results also further illustrate the importance of expansion tests under actual mechanical constraints to probe the thermal expansion characteristics of the cell. Additionally, to further analyze the thermal expansion degree and its SOC correlation in practical cell operation, we designed 1 C charge and 1.5 C discharge expansion tests with or without TR. As shown in Fig. 10(c and d), the increasing swelling of 2.16% is caused by TR of 2.28% at the end of the charge, while it decreases by 4.34% due to TR of 1.21% at the end of the discharge. These results further prove the thermal contraction phenomenon at low SOC, which only applies without mechanical constraints. These conclusions provide a basis for understanding the thermal-mechanical coupling behavior and elucidate the need for experiment design under mechanical constraints.

4.3. Quantification analysis of multi-field coupling

In multi-field coupling problems, because of the complexity and diversity of coupling relationships, the degree of correlation and dependence between two fields must be further quantified. Fig. 11(a–d) shows normalized MIC and MRC between characteristic parameters and fields, such as T and σ. In Fig. 11(a), all electrochemical parameters exhibit a temperature correlation of more than 0.6 Temp@MIC, except for Q^+_{max}, but mechanical parameters have the weakest correlation with temperature. In Fig. 11(c), an interesting phenomenon is that all mechanical parameters are highly related to pressure, while Pres@MIC between pressure and electrochemical parameters is less than 0.6. Although MIC-based correlation evaluation indicates the existence of some connection between the two fields, the extent of their interaction is not yet characterized, which is the key to assessing the reliability of battery performance and robustness of estimation algorithms. For the coupling intensity analysis, as described in Fig. 11(b), the temperature-induced characteristic parameters by Temp@MRC can be divided into three levels. (1) The first level is all kinetic parameters, except for R_o; (2) the second level consists of η_{max}, R_o, and all mechanical parameters, except for $\Delta\delta_s$; and (3) the third

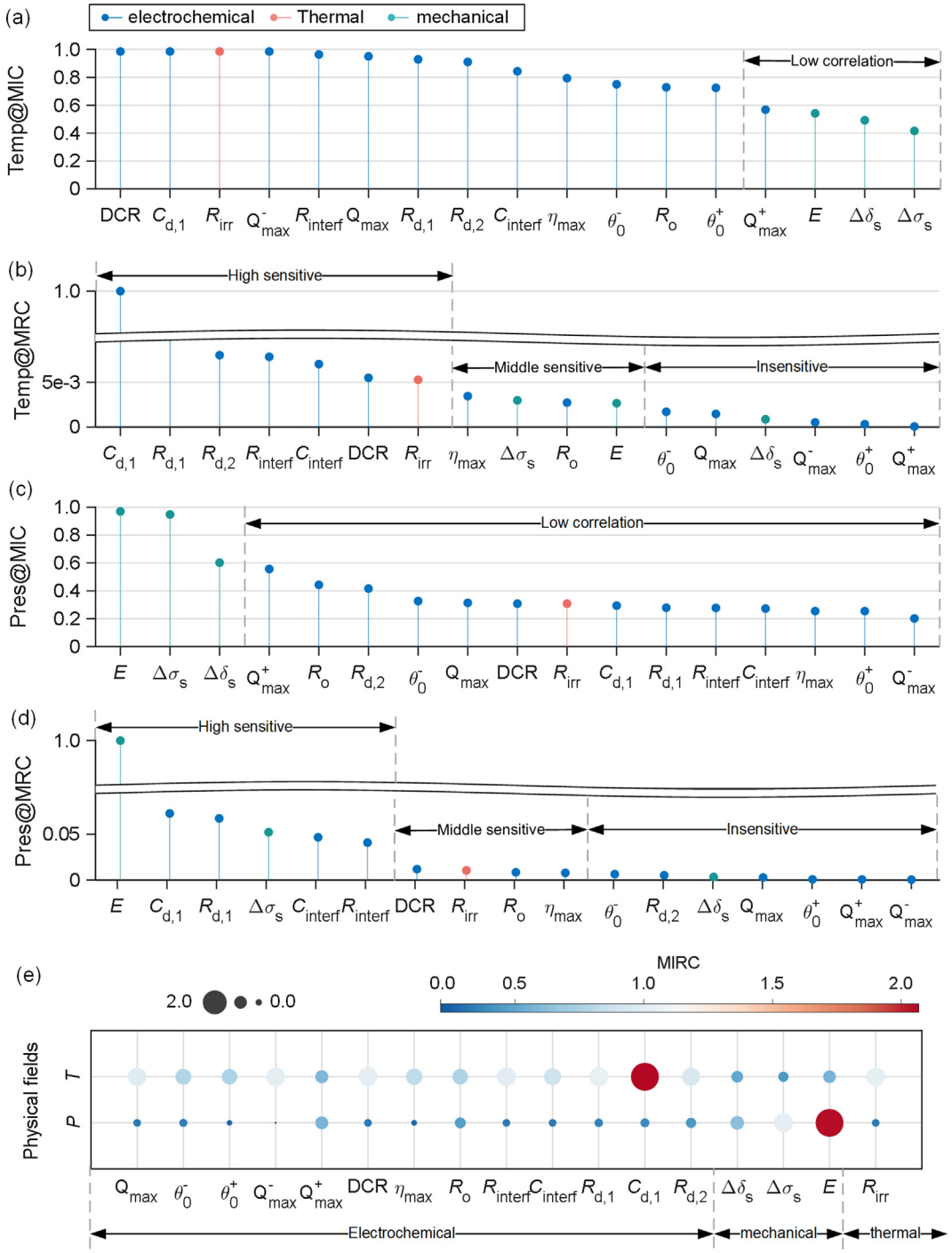

Fig. 11. (a) Normalized MIC and (b) MRC for temperature-induced parameters. (c, d) Pressure-induced parameters. (e) Bubble plot for quantification of multi-field coupling by composite MIRC. The parameters are categorized into three types: electrochemical, mechanical, and thermal parameters.

level includes all thermodynamic parameters, Q_{max}, and $\Delta\delta_s$. Similarly, the pressure-induced characteristic parameters, according to Pres@MRC, are also categorized into three levels. (1) The first level is made up of all mechanical parameters except for $\Delta\delta_s$ and all kinetic parameters except for R_o; (2) the second level consists of DCR, R_{irr}, and η_{max}; and (3) the third level includes $\Delta\delta_s$, $R_{d,2}$ from solid diffusion, and all thermodynamic parameters. Through the above ranking and grading, we can gain the following conclusions and application inspirations.

(1) The extent to the electrochemical reactions affected by temperatures is in the following order: $R_{d,1} > R_{d,2} > R_{interf} > R_o$, while the influence of pressure on reaction kinetics is as follows: $R_{d,1} > R_{interf} > R_o > R_{d,2}$. Therefore, improving the temperature properties of the electrolyte and the active area of the solid-liquid reaction interface is an effective way to enhance the capacity and power performance of the battery.
(2) Whether thermal or mechanical field, thermodynamic parameters and $\Delta\delta_s$, lying in the third echelon, are

insensitive parameters from the equilibrium potential of the electrode and cell swelling thickness. In cloud BMS, these insensitive profiles can be calibrated as benchmark curves and then applied in degradation trajectory analysis and battery fault diagnosis.

(3) For mechanical parameters, $\Delta\delta$ has a low temperature and pressure sensitivity, while $\Delta\sigma$ has a high pressure and moderate temperature sensitivity. In practical applications, pressure signals are more accessible than strain sensors with low accuracy. Thus, it is more reasonable to establish a high-precision mechanical model with pressure as input and strain as output, which helps estimate irreversible expansion and diagnose battery faults.

(4) As shown in Fig. 11(e), the bubble sizes of the combined metrics indicate that the thermal-electrical coupling of the battery is more intense than the other two-field couplings during the battery operation. This conclusion helps to design the decoupling experiments and develop identification methods in multi-field coupling models, ensuring the reliability of BMS functions during the realistic operation of electric vehicles.

4.4. Future work and applications

In the future, we aim to expand the scope and conclusions of this work in various directions, one of which is establishing the battery multi-field coupling modeling under mechanical constraints. A main step would be applying test platforms with constant mechanical pressure or known module stiffness to eliminate the mechanical coupling degree as much as possible, contributing to the downscaling of the three-field to two-field coupling problem, thereby constructing the correlation between a single field and electrochemical parameters. To identify the parameters that are valid for a large operating pressure range, the battery testing procedures need to be expanded for coupling tests under various mechanical constraints. Furthermore, the decoupling identification method needs to be further developed to construct a digital twin model of the battery for dynamic co-simulation. Another key expansion to the framework is investigating multi-field coupling behavior under abusive conditions, e.g., lithium plating, internal short circuits, and overcharging. The substantial heat and gas production due to side reactions causes drastic changes in voltage, temperature, and mechanical signals. Multi-field coupling analysis contributes to the exploration of the potential of multi-physical signals in non-invasive fault diagnosis.

5. Conclusions

Lithium-ion batteries exhibit complex interactions among electrochemical, thermal, and mechanical fields, adversely affecting their safety and longevity. However, understanding multi-field coupling behavior is constrained by its inherent complexity and the limitations of measurement techniques. This work aimed to resolve this issue by proposing analytical approaches that integrate constraint-based experiments with an in-situ quantitative framework. Multi-physics signals were directly measured under three types of mechanical constraints, creating a comprehensive characterization dataset. Within the proposed in-situ quantitative framework, this dataset was used to reveal multi-field coupling mechanisms, isolate the effects of SOC, temperature, and pressure on mechanical behavior, and quantify the coupling degree among multi-physics.

Revealed coupling mechanism via equivalent circuit models. The results showed a strong dependence of coupling behavior on cell electrochemistry. The temperature resulted in a varied degree of pressure-induced impedance due to the changed key controlling step, contributing to the different effects of heat generation and performance improvement by applying pressure on the battery. The temperature-dependence optimal pressure ranges (180 to 240 kPa at 10 °C, 100 to 150 kPa at 25 °C, 50 to 100 kPa at 40 °C) were further proven by the variation of interfacial impedance representing the active surface area. For mechanical behavior, the estimated elastic modulus demonstrates the two most influencing factors, pressure and SOC, which led to the evolution of expansion force under different conditions due to stiffness property and the host phase transitions. Mechanical constraints resulted in varied thermal expansion due to increased elastic modulus with temperature at 20% SOC for thermal-induced mechanical behavior, contributing to the swelling force of 1.6% per unit of elevated temperature during lithiuation process.

Mechanical interpretability by differential analysis. Mechanical behavior was non-invasively characterized by differential voltage and swelling curves, coupled with the electrode equilibrium potential, thereby assigning swelling peaks to corresponding phase transitions during lithiation/de-lithiation. For mechanical pressure, the declined swelling peaks of the phase transition related to SiO_x and NCM811 led to the reduction of expansion thickness. However, the increasing swelling peaks with temperature result in increased expansion due to the phase transitions related to Gr and NCM811.

Quantitative assessment of coupling correlation and strength. Quantification results show that electrochemical parameters have a high correlation with temperature because of the ranking order of the maximum information coefficient, while mechanical parameters strongly correlate to pressure. The higher maximum change rate of temperature than pressure for all electrochemical parameters suggests the highest coupled degree of electrochemical-thermal field.

This work highlights the potential of the analytical procedures for visualizing and quantifying multi-field coupling, offering deeper insights into the coupled interaction mechanisms and providing solutions for multi-field simulation. These advancements will inevitably guide the improvement of battery performance and the development of BMS in practical applications.

Abbreviations

LIBs	Lithium-ion batteries	MRC	Maximum rate of change
BMSs	Battery management systems	SOC	State of charge
FSM	Free stack mode	DCR	Direct current resistance
CPM	Constant pressure mode	OCV	Open circuit voltage
CDM	Constant displacement mode	RMSE	Root-mean-square error
EMs	Electrochemical models	TEP	Thermal expansion pressure
ECMs	Equivalent circuit models	TED	Thermal expansion displacement
EIS	Electrochemical impedance spectrum	DSQ	Differential swelling versus capacity
TR	Temperature rise	DVQ	Differential voltage versus capacity
NCM811	$LiNi_{0.8}Co_{0.1}Mn_{0.1}O_2$	MIRC	The sum of MIC and MRC
Gr-SiO_x	Composite anode of graphite and silicon oxide	MI	Mutual information
CC	Constant current	DPQ	Differential pressure versus capacity
CV	Constant voltage	DDQ	Differential pressure versus capacity
MIC	Maximum information coefficient	DSV	Differential swelling versus voltage

CRediT authorship contribution statement

Xue Cai: Conceptualization, Data curation, Investigation, Methodology, Software, Validation, Visualization, Writing – original draft. **Caiping Zhang:** Conceptualization, Funding acquisition, Methodology, Supervision, Writing – review & editing. **Zeping Chen:** Validation, Investigation, Resources. **Linjin Zhang:** Conceptualization, Investigation, Methodology. **Dirk Uwe Sauer:** Methodology, Resources, Validation, Writing – review & editing, Supervision. **Weihan Li:** Conceptualization, Methodology, Resources, Supervision, Writing – review & editing.

Declaration of competing interest

The authors declare that they have no known competing financial interests or personal relationships that could have appeared to influence the work reported in this paper.

Acknowledgments

This work was supported by the National Science Fund for Excellent Youth Scholars of China (52222708) and the National Natural Science Foundation of China (51977007). The authors would like to thank Sascha Berg and Egbert Figgemeier from RWTH Aachen University for their support in electrochemical impedance analysis and review.

Appendix A. Supplementary material

Supplementary material to this article can be found online at https://doi.org/10.1016/j.jechem.2024.03.048.

References

[1] J. Xiao, F. Shi, T. Glossmann, et al., Nat. Energy 8 (2023) 329–339.
[2] C. Yuan, Y. Hahn, W. Lu, et al., Cell Rep. Phys. Sci. 3 (2022) 101158.
[3] J. Wu, M. Zheng, T. Liu, et al., Energy Storage Mater. 54 (2023) 120–134.
[4] F. Duffner, N. Kronemeyer, J. Tübke, et al., Nat. Energy 6 (2021) 123–134.
[5] X. Zhang, T. Zhang, N. Liu, et al., Eng. Fail. Anal. 154 (2023) 107653.
[6] V. Müller, R.-G. Scurtu, M. Memm, et al., J. Power Sources 440 (2019) 227148.
[7] X. Du, Y. Hu, S.-Y. Choe, et al., J. Power Sources 573 (2023) 233117.
[8] K.-Y. Oh, B.I. Epureanu, J. Power Sources 303 (2016) 86–96.
[9] Y. Wang, R. Ni, X. Jiang, et al., Appl. Energy 347 (2023) 121444.
[10] A. Nyman, M. Behm, G. Lindbergh, Electrochimica Acta 53 (2008) 6356–6365.
[11] W. Ai, L. Kraft, J. Sturm, et al., J. Electrochem. Soc. 167 (2020) 013512.
[12] P. Luo, P. Li, D. Ma, et al., J. Electrochem. Soc. 169 (2022) 100535.
[13] E. Kwak, D.S. Son, S. Jeong, et al., J. Energy Storage 28 (2020) 101269.
[14] P. Mohtat, S. Lee, J.B. Siegel, et al., J. Electrochem. Soc. 168 (2021) 100520.
[15] E. Kwak, S. Jeong, J. Kim, et al., J. Power Sources 483 (2021) 229079.
[16] T. Deich, S.L. Hahn, S. Both, et al., J. Energy Storage 28 (2020) 101192.
[17] M. Wünsch, J. Kaufman, D.U. Sauer, J. Energy Storage 21 (2019) 149–155.
[18] J. Cannarella, C.B. Arnold, J. Power Sources 245 (2014) 745–751.
[19] A.S. Mussa, M. Klett, G. Lindbergh, et al., J. Power Sources 385 (2018) 18–26.
[20] X.M. Liu, C.B. Arnold, J. Electrochem. Soc. 163 (2016) A2501.
[21] D. Sauerteig, N. Hanselmann, A. Arzberger, et al., J. Power Sources 378 (2018) 235–247.
[22] Y. Chen, L. Yang, F. Guo, et al., J. Power Sources 527 (2022) 231178.
[23] M. Ecker, T.K.D. Tran, P. Dechent, et al., J. Electrochem. Soc. 162 (2015) A1836–A1848.
[24] L. Wu, Z. Lyu, Z. Huang, et al., J. Energy Chem. 89 (2024) 27–40.
[25] Y. Jiang, J. Xu, W. Hou, et al., Energy 221 (2021) 119804.
[26] Y. Jiang, J. Xu, C. Jin, et al., J. Energy Storage 70 (2023) 107916.
[27] L. Hovestadt, K. Wildermann, A. Sahhary, et al., J. Electrochem. Soc. 167 (2020) 110540.
[28] K.-Y. Oh, B.I. Epureanu, Appl. Energy 178 (2016) 633–646.
[29] J. Zhu, W. Xu, M. Knapp, et al., Cell Rep. Phys. Sci. 4 (2023) 101464.
[30] A. Chen, W. Zhang, C. Zhang, et al., IEEE Trans. Ind. Electron. 67 (2020) 9492–9502.
[31] H. Ruan, B. Sun, J. Jiang, et al., Electrochimica Acta 394 (2021) 139066.
[32] Z. Liu, C. Wang, X. Guo, et al., J. Power Sources 506 (2021) 230205.
[33] L. De Sutter, G. Berckmans, M. Marinaro, et al., J. Power Sources 451 (2020) 227774.
[34] L.A. Berla, S.W. Lee, Y. Cui, et al., J. Power Sources 273 (2015) 41–51.
[35] Y. Jiang, G. Offer, J. Jiang, et al., J. Electrochem. Soc. 167 (2020) 130533.
[36] F.B. Spingler, S. Kücher, R. Phillips, et al., J. Electrochem. Soc. 168 (2021) 040515.
[37] X. Wang, Y. Song, H. Cui, et al., ENERGY Environ. Mater. 6 (2023) e12401.
[38] C.-C. Lin, H.-Y. Liu, J.-W. Kang, et al., Energy Storage Mater. 51 (2022) 159–171.
[39] A.J. Louli, J. Li, S. Trussler, et al., J. Electrochem. Soc. 164 (2017) A2689–A2696.
[40] H. Pegel, O. Von Kessel, P. Heugel, et al., J. Power Sources 537 (2022) 231443.
[41] P. Kargl, V. Drews, P. Daubinger, et al., J. Power Sources 548 (2022) 232042.
[42] J. Miranda, G. Franklin, T.S. Mathis, et al., Energy Storage Mater. 65 (2024) 103105.
[43] B. Rieger, S. Schlueter, S.V. Erhard, et al., J. Energy Storage 6 (2016) 213–221.
[44] G. Fan, D. Lu, M.S. Trimboli, et al., J. Power Sources 557 (2023) 232555.
[45] D. Clerici, F. Mocera, A. Somà, J. Power Sources 542 (2022) 231735.
[46] W. Mei, Q. Duan, W. Lu, et al., J. Clean. Prod. 274 (2020) 122643.
[47] X. Jia, C. Zhang, L.Y. Wang, et al., J. Electrochem. Soc. 167 (2020) 020503.
[48] O. Von Kessel, T. Deich, S. Hahn, et al., J. Power Sources 508 (2021) 230337.
[49] D.N. Reshef, Y.A. Reshef, H.K. Finucane, et al., Science 334 (2011) 1518–1524.
[50] J.B. Kinney, G.S. Atwal, Proc. Natl. Acad. Sci. 111 (2014) 3354–3359.
[51] R. Li, W. Li, A. Singh, et al., Energy Storage Mater. 52 (2022) 395–429.
[52] A. Barai, R. Tangirala, K. Uddin, et al., J. Energy Storage 13 (2017) 211–219.
[53] J. Zhang, H. Huang, J. Sun, Powder Technol. 409 (2022) 117828.
[54] L. Savignac, J.I.G. Dawkins, S.B. Schougaard, et al., Electrochem. Commun. 125 (2021) 106979.
[55] N. Piao, X. Gao, H. Yang, et al., eTransportation 11 (2022) 100145.
[56] R. Fang, Z. Li, J. Electrochem. Soc. 169 (2022) 090515.
[57] R. Fang, Z. Li, J. Electrochem. Soc. 168 (2021) 120523.
[58] S. Müller, P. Pietsch, B.-E. Brandt, et al., Nat. Commun. 9 (2018) 2340.
[59] J. Xu, E. Hu, D. Nordlund, et al., ACS Appl. Mater. Interfaces 8 (2016) 31677–31683.
[60] F. Grimsmann, F. Brauchle, T. Gerbert, et al., J. Energy Storage 12 (2017) 132–137.